Mon. Not. R. Astron. Soc. **000**, 1–21 (2012) Printed 22 April 2014 (MN LATEX style file v2.2)

Weighing the Giants II: Improved Calibration of Photometry from Stellar Colors and Accurate Photometric Redshifts

Patrick L. Kelly[1,2,3,4] ⋆, Anja von der Linden[1,2], Douglas E. Applegate[1,2,3], Mark T. Allen[1,2], Steven W. Allen[1,2,3], Patricia R. Burchat[1,2], David L. Burke[1,3], Harald Ebeling[5], Peter Capak[6], Oliver Czoske[7], David Donovan[5], Adam Mantz[8], and R. Glenn Morris[1,3]

[1]*Kavli Institute for Particle Astrophysics and Cosmology, Stanford University, 452 Lomita Mall, Stanford, CA 94305-4085, USA*
[2]*Department of Physics, Stanford University, 382 Via Pueblo Mall, Stanford, CA 94305-4060, USA*
[3]*SLAC National Accelerator Laboratory, 2575 Sand Hill Road, Menlo Park, CA 94025, USA*
[4]*Department of Astronomy, University of California, Berkeley, CA 94720-3411, USA*
[5]*Institute for Astronomy, 2680 Woodlawn Drive, Honolulu, HI 96822, USA*
[6]*California Institute of Technology, MC 249-17, 1200 East California Boulevard, Pasadena, CA 91125, USA*
[7]*Universität Wien, Institut für Astronomie, Türkenschanzstraße 17, 1180 Wien, Austria*
[8]*Kavli Institute for Cosmological Physics, University of Chicago, 5640 South Ellis Avenue, Chicago, IL 60637-1433, USA*

ABSTRACT

We present improved methods for using stars found in astronomical exposures to calibrate both star and galaxy colors as well as to adjust the instrument flat field. By developing a spectroscopic model for the SDSS stellar locus in color-color space, synthesizing an expected stellar locus, and simultaneously solving for all unknown zeropoints when fitting to the instrumental locus, we increase the calibration accuracy of stellar locus matching. We also use a new combined technique to estimate improved flat-field models for the Subaru SuprimeCam camera, forming 'star-flats' based on the magnitudes of stars observed in multiple positions or through comparison with available measurements in the SDSS catalog. These techniques yield galaxy magnitudes with reliable color calibration ($\lesssim$ 0.01 - 0.02 mag accuracy) that enable us to estimate photometric redshift probability distributions without spectroscopic training samples. We test the accuracy of our photometric redshifts using spectroscopic redshifts z_s for ∼5000 galaxies in 27 cluster fields with at least five bands of photometry, as well as galaxies in the COSMOS field, finding $\sigma((z_p - z_s)/(1 + z_s)) \approx 0.03$ for the most probable redshift z_p. We show that the full posterior probability distributions for the redshifts of galaxies with five-band photometry exhibit good agreement with redshifts estimated from thirty-band photometry in the COSMOS field. The growth of shear with increasing distance behind each galaxy cluster shows the expected redshift-distance relation for a flat Λ-CDM cosmology. Photometric redshifts and calibrated colors are used in subsequent papers to measure the masses of 51 galaxy clusters from their weak gravitational shear and determine improved cosmological constraints. We make our Python code for stellar locus matching publicly available at http://big-macs-calibrate.googlecode.com; the code requires only input catalogs and filter transmission functions.

Key words: methods: observational – techniques: photometric – galaxies: clusters – gravitational lensing: weak.

1 INTRODUCTION

A principal challenge for current and planned optical and near-IR wide-field surveys is to estimate accurate redshift probability distributions for millions of galaxies from broadband photometry. Correct probability distributions are necessary, for example, for the weak lensing cosmological measurements that current and upcoming surveys (e.g., Dark Energy Survey; Large Synoptic Survey Telescope) aim to extract from wide-field optical imaging. Photometric redshift algorithms, however, can show significant systematic biases if the input galaxy photometry has even modest (∼0.03-0.04 mag) calibration error. To infer the weak lensing masses of galaxy clusters using photometric redshifts estimated from Subaru and CFHT photometry, we have developed and applied sev-

⋆ E-mail:pkelly@astro.berkeley.edu

eral techniques to calibrate broadband galaxy colors to an accuracy of ∼0.01-0.02 magnitudes, without requiring specific standard star observations.

The relative distribution of counts recorded during flat-field exposures of an illuminated screen or of the sky can differ from the actual instrument sensitivity by up to ∼10% across the focal plane (Manfroid et al. 2001; Koch et al. 2003; Magnier & Cuillandre 2004; Capak et al. 2007; Regnault et al. 2009) because of a combination of geometric distortion, superposed reflections, and imperfect flat-field sources. We combine two methods to measure the Subaru SuprimeCam 'star flat,' the map of the spatially dependent zeropoint error that remains after traditional flat-field correction, across a decade of observations and camera upgrades. Our star-flat model is informed by the magnitudes of the same stars observed in multiple locations on the focal plane, as well as by comparisons with available SDSS catalog magnitudes.

A powerful color calibration strategy suitable for use with medium-to-wide field data uses the fact that almost all of the stars observed in any field lie along a well-understood one-dimensional locus in color-color space (e.g., High et al. 2009; MacDonald et al. 2004). According to this technique, the zeropoints of the filters are shifted until the position of the observed stellar locus matches the expected locus. The resulting calibration automatically corrects for Milky Way dust extinction. We improve the accuracy of this technique by constructing a spectroscopic model for the SDSS stellar locus, and by developing a numerical algorithm that fits for all unknown zeropoints simultaneously.

Comparison of photometric redshifts estimated from our calibrated galaxy magnitudes against spectroscopic redshifts show that these bootstrapped calibration techniques are effective. We find excellent agreement between the most probable photometric redshift z_p and the spectroscopic redshift z_s, with a measurement error of $\sigma((z_p - z_s)/(1 + z_s)) \approx 0.03$. Five-band $p(z)$ distributions summed over different sets of galaxies ($\sum_{\rm gal} p(z)$) show congruence with the Ilbert et al. (2009) 30-band photometric redshift distributions for the same sets of galaxies. The growth of lensing shear with increasing redshift of galaxies behind each cluster, sensitive to the photometric redshifts of galaxies too faint to be represented in spectroscopic samples, exhibits the shape expected for a flat Λ-CDM cosmology.

The algorithms and techniques described in this paper may be useful as a primary means of calibration or as a demanding test of zeropoint accuracy. This paper is the second in a series ("Weighing the Giants") addressing the specific task of measuring accurate galaxy cluster masses using shear-based weak lensing methods. Paper I (von der Linden et al. 2012) in this series describes the overall project strategy, the cluster sample and the data reduction methods. Paper III (Applegate et al. 2012) presents a Bayesian approach to measuring galaxy-cluster masses, that uses the full photometric redshift probability distributions reported here; these masses are compared to those measured with a standard 'color-cut' method based on three-filter photometry for each field.

Section 2 of this paper summarizes the wide-field imaging data used here. In Section 3, we describe how we determine the SuprimeCam star flats, which we use to extract consistent magnitudes across the CCD array. Section 4 describes the stellar locus calibration algorithm and the spectroscopic model we have developed for the stellar locus. In Section 5, we discuss the algorithms and the templates for galaxy spectra that we use to estimate photometric redshift probability distributions $p(z)$. A method for finding the zeropoints of u^*- and B_J- band photometry is presented in Section 6. In Section 7, we use the galaxy cluster red sequence and spectroscopic redshift measurements in the cluster fields to evaluate the accuracy of our photometric calibrations and redshift estimates. In Section 7.3, we compare the redshift probability distributions determined from calibrated photometry in five bands ($B_J V_J r^+ i^+ z^+$) against both the zCOSMOS spectroscopic redshift sample and the most probable redshift inferred from thirty imaging bands in the COSMOS field. General agreement between the observed growth of weak lensing shear with distance behind the massive clusters and the Λ-CDM expectation is found in Section 8. In Section 9, we summarize the calibration techniques and the quality of the photometric redshift estimates.

2 SUBARU AND CFHT IMAGING DATA

Our imaging data set consists of wide-field optical exposures of 51 X-ray–luminous galaxy clusters that span the redshift interval $0.15 < z < 0.7$. The data were acquired between 2000 and 2009 with SuprimeCam mounted on the 8.3-meter Subaru telescope and with MegaPrime on the 3.6-meter Canada-France-Hawaii telescope (CFHT). The field of view of SuprimeCam is $34' \times 27'$ ($0.2''$ pixel^{-1}), while the MegaPrime has a $1^\circ \times 1^\circ$ field of view ($0.187''$ pixel^{-1}). Each cluster field was imaged in at least three separate broadband filters, and 27 fields were imaged with five or more SuprimeCam ($B_J V_J R_C I_C z^+$) or MegaPrime ($u^* g^* r^* i^* z^*$) bandpasses. Paper I describes the cluster sample and observations, the overscan, bias, and dark corrections, as well as the flat-field and superflat processing steps.

3 MEASURING THE STAR FLAT

The intensity of a pixelated image recorded by a CCD camera mounted on a telescope depends, in part, on the properties of the CCD sensors and the readout electronics, as well as the illumination of the focal plane by the telescope optics. Correcting images for spatial sensitivity variations is necessary to be able to extract accurate fluxes for galaxies and stars.

Calibration images of illuminated dome screens, the twilight sky, and the night sky vary smoothly on scales of tens of arcseconds, and these exposures of flat-field sources are useful for measuring local pixel-to-pixel sensitivity variations. The variation of 'flat-field' images taken with a wide-field camera on several arcminute scales, however, can disagree with the camera's actual sensitivity to point sources. The discrepancy can be up to ∼10% across the field of view of wide-field instruments (Manfroid et al. 2001; Koch et al. 2003; Magnier & Cuillandre 2004; Capak et al. 2007; Regnault et al. 2009). Dividing wide-field science images by flat-field exposures leads to objects near the center of the focal plane that are systematically fainter than sources at the periphery.

Geometric distortion along the optical paths of many wide-field telescopes, such as Subaru/SuprimeCam and CFHT/MegaPrime, results in a decrease in pixel scale with increasing distance from the center of the focal plane. In SuprimeCam, the pixel scale decreases by ∼1.5% between the center and $15'$ from the center, with a corresponding decrease of ∼3% in the solid angle subtended by a pixel. (See Fig. 3 in Paper I.) This effect means that pixels near the center of the field will receive proportionally greater flux than they otherwise would when illuminated by a hypothetical calibration source with constant flux per unit solid angle. The effect of variation in pixel solid angle due to geometric distortion can be explicitly corrected using the

Jacobian of the astrometric distortion (e.g., Capak et al. 2007), or left for correction by a 'star flat' (e.g., Regnault et al. 2009), which is the approach we take.

Light that scatters off the surfaces of reflective and refractive optical elements also contributes to the spatial distribution of counts in flat-field images. On average, photons scattering from filters and the CCD sensors are redirected toward the field center (e.g., Regnault et al. 2009). This can be seen, for example, in the halos that surround bright stars. Stellar halos, which are due to extra reflections, are each centered on a point that is offset from the star towards the center of the field of view. For diffuse sources that extend across the field of view, such as dome screens or the night sky, a continuum of superposed reflections accumulates near the center of the exposure.

Light baffles for wide-field instruments can only be modestly effective. Capak et al. (2007) showed that the intensity of a SuprimeCam flat field varies by ±5% in the corners of the focal plane due to light scattered from outside the field of view and that the intensity of scattered light depends on the position of the telescope and whether exposures were taken in dark or twilight conditions. To reduce our susceptibility to these intensity variations in the periphery, we exclude regions of the sensors that are more than 15′ from the center of the field.

Zeropoint variations across the focal plane that remain after dividing images by flat-field exposures can be measured with two approaches. A first technique is to image the same set of stars at different positions in the focal plane by dithering the telescope or rotating the camera, and find the spatially dependent corrections (the 'star flat') that result in the smallest dispersion in magnitudes for each star measured in different positions (Manfroid et al. 2001; Magnier & Cuillandre 2004; Capak et al. 2007; Padmanabhan et al. 2008; Regnault et al. 2009; and Wittman et al. 2012). A second approach is to compare the measured magnitudes of stars to those in photometrically consistent catalogs, such as the SDSS catalogs (Koch et al. 2003). We apply both approaches and describe the process in detail below.

The CFHT ELIXIR pipeline fits and corrects for a star flat for MegaPrime observations (Magnier & Cuillandre 2004), so we measure only the SuprimeCam star flat across nine years of observations. In addition to spatially varying zeropoint corrections, Regnault et al. (2009) find evidence for position-dependent color terms across the CFHT MegaPrime field of view, which the authors attribute to an angular dependence of the transmission function for interference filters.

3.1 Chip Configurations: SuprimeCam Sensor and Electronics Upgrades

We have grouped our 2000-2009 SuprimeCam images into successive periods that correspond to upgrades of the CCD array (see Table 3 of Paper I). The CCD sensors in the early 8- and 9-chip configurations exhibited nonlinear response. We were able to correct the nonlinearity except for two MIT/Lincoln CCD sensors in configuration 8 and three MIT/Lincoln CCD sensors in configuration 9, which we discarded. The '10_1' and '10_2' configurations, installed March 27, 2001, feature ten MIT/Lincoln CCD sensors with fewer cosmetic defects and linear response below saturation. The upper left chip had lower quantum efficiency than the other CCDs, but this can be corrected by the flat field. The last set, the '10_3' configuration installed in July 2008, consists of ten Hamamatsu Photonics CCD sensors.

3.2 Flat-Field Correction Applied to Subaru Imaging

Before fitting for the SuprimeCam star flat, we divide each image by a stack of dome-flat or twilight-flat exposures taken during the same observing run (or adjacent runs if few flats are available), and then by a heavily smoothed stack of night-sky flats (or 'superflat'). Flat images are normalized by their median pixel value before being stacked. The night-sky flat is constructed from object-subtracted, smoothed exposures, already divided by the stacked dome or twilight flats, with no bright stars or strong internal reflections (see Erben et al. 2005) and typically varies by (0.5-1.5)% across the field of view. While the stack of dome-flat or twilight-flat exposures corrects pixel-to-pixel sensitivity variations, the smoothed night-sky superflat makes adjustments for larger-scale features.

3.3 Dither Patterns and Camera Rotations

Telescope dithers or camera rotations that move stars substantial distances across the focal plane are helpful to constrain spatial zeropoint variation. The 34′x27′ SuprimeCam exposures that we analyze have dither patterns that generally vary by a relatively modest angle of 1′ to 2′. For Subaru images that we took to measure the masses of the MACS (Ebeling et al. 2001; Ebeling et al. 2007; Ebeling et al. 2010) galaxy clusters, we rotated the camera by 90° to facilitate star-flat fits. Subaru images that were taken by other groups and included in our analysis, which we accessed through the Subaru-Mitaka-Okayama-Kiso Archive (SMOKA)[1] (Baba et al. 2002), can have different dither sequences and rotations (e.g., rotations of 45° or no rotation).

3.4 Measuring the Star Flat

We perform a separate star-flat fit to each of 471 sets of exposures corresponding to a given cluster field, filter, and observing run (e.g., Abell 68, B_J, 18 July 2007). The median number of exposures we use each star-flat fit is six, with a typical relative rotation of 90° after the first three exposures.

3.4.1 Selecting the Star Sample

To select stars, we choose objects that the SExtractor (Bertin & Arnouts 1996) neural network classifier, supplied with the image seeing (SEEING_FWHM), suggests are stellar-like (i.e., where CLASS_STAR > 0.65). We also admit only those star candidates for which the flux within 2.5 Kron (1980) radii (MAG_AUTO) has less than 0.1 mag uncertainty, as well as where the stellar image is unblended, has no bad or saturated pixels, has no bright neighbors, and is not truncated by a CCD sensor boundary (i.e., we include only objects with FLAG=0). To exclude objects that are saturated or affected by detector nonlinearity in our images, we include only measurements of objects with a maximum pixel value less than 25,000 ADU above the ~10,000 ADU bias level, well below the full-well capacity of ~35,000 ADU above the bias level. Both for fitting the star flats and for measuring galaxy photometry and shapes for the analysis of weak lensing, we exclude objects in each catalog that are more than 15′ from the center of the field. To identify and remove exceptionally discrepant magnitudes early, we use objects that appear in different exposures to estimate the

[1] http://smoka.nao.ac.jp/

relative zeropoint of each exposure, and subtract these zeropoints from the magnitude measured for each object. For each star candidate, we remove any magnitude measurements $m_{\rm star}^{\rm exp}$ for which $|m_{\rm star}^{\rm exp} - {\rm median}(m)| > 1$ mag, where median(m) is the median of magnitudes $m_{\rm star}^{\rm exp}$ across all exposures.

3.4.2 Star-flat Model

We model the SuprimeCam position-dependent zeropoint with a spatially varying function $C(x, y, {\rm chip}, {\rm rotation})$, which is the sum of a separate function $f(x, y)_{\rm rot}$ for each rotation of the camera and a single set of chip-dependent offsets $O_{\rm chip}$, shared across the rotations and dithered exposures:

$$C(x, y, {\rm chip}, {\rm rotation}) = f(x, y)_{\rm rot} + O_{\rm chip}, \quad (1)$$

where $f(x, y)_{\rm rot}$ is the product of third-order Chebyshev polynomials in x and y coordinates on the focal plane.

For the stars in each exposure that meet the sample criteria, we express the measured magnitude of each star, $m_{\rm star}^{\rm exp}$, in terms of the spatially varying correction $C(x, y, {\rm chip}, {\rm rotation})$, and a magnitude $m_{\rm star}^{\rm model}$, which is a free parameter in the fit and corresponds to the stellar magnitude that would be measured if the exposures had no position-dependent zeropoint variation:

$$m_{\rm star}^{\rm exp} = C(x, y, {\rm chip}, {\rm rotation}) + ZP_{\rm exp} + m_{\rm star}^{\rm model}, \quad (2)$$

where $ZP_{\rm exp}$ is the zeropoint for each exposure.

We also introduce constraints from available magnitudes from photometrically consistent catalogs. These are SDSS magnitudes or, alternatively, SuprimeCam or MegaPrime magnitudes corrected by a previous successful star-flat fit. We express each available catalog magnitude $m_{\rm star}^{\rm cat}$ in terms of the modeled magnitude $m_{\rm star}^{\rm model}$, a zeropoint offset $O_{\rm cat}$, and a color term $\mathcal{S}_{\rm cat} \times c_{\rm star}^{\rm cat}$:

$$m_{\rm star}^{\rm cat} = m_{\rm star}^{\rm model} + O_{\rm cat} - \mathcal{S}_{\rm cat} \times c_{\rm star}^{\rm cat}. \quad (3)$$

The star color $c_{\rm star}^{\rm cat}$ is calculated from catalog magnitudes (e.g., $g' - r'$). We find the coefficient $\mathcal{S}_{\rm cat}$ of the color term before fitting for the other star-flat parameters.

The free parameters in the model are the coefficients in the Chebyshev polynomials in $f(x, y)_{\rm rot}$ for each camera rotation, $O_{\rm chip}$, $O_{\rm cat}$, $ZP_{\rm exp}$, and, for each star, $m_{\rm star}^{\rm model}$.

3.4.3 Fitting Procedure

We construct a set of linear equations from two sets of equations: Equation 2 for each observation of each stellar candidate, and Equation 3 for each star with a catalog magnitude. The matrix representing the system of equations where each equation corresponds to a row is sparse because only a handful of equations include $m_{\rm star}^{\rm model}$ for each star. Each row in the matrix is weighted by the inverse-square of the uncertainty in $m_{\rm star}^{\rm exp}$ or $m_{\rm star}^{\rm cat}$. When the statistical uncertainty is less than 0.04 mag, we set the uncertainty to be 0.04 mag for purposes of the fit, so that a small number of objects will not dominate the solution. We use CXSparse (Davis 2006), a C library for sparse matrix algebra, to apply a QR decomposition computed with a Householder transformation.

After computing an inital solution, measured magnitudes $m_{\rm star}^{\rm exp}$ that are more than 5σ from the corresponding model magnitudes $m_{\rm star}^{\rm model}$ are removed. We then refit the remaining measured and catalog magnitudes, $m_{\rm star}^{\rm exp}$ and $m_{\rm star}^{\rm cat}$.

When fewer than 400 stars in the exposure have a catalog magnitude $m_{\rm star}^{\rm cat}$, we remove linear terms in the Chebyshev polynomials in $f(x, y)_{\rm rot}$ because the set of exposure zeropoints $O_{\rm chip}$ exhibit a degeneracy with the linear Chebyshev terms. Consider, for example, exposures taken after three successive telescope dithers to the north by 1′. If all stars show fluxes that diminish by 10% with each consecutive exposure, these changes in flux could reflect either worsening atmospheric transparency (i.e., $ZP_{\rm exp}$) or a linear spatial gradient in the camera's sensitivity. The addition of a sufficient number of $m_{\rm star}^{\rm cat}$ magnitudes from an external photometrically consistent catalog for stars spanning the field of view, however, breaks this degeneracy.

3.4.4 Evaluating the Star-Flat Fit to Each Set of Exposures

To identify star-flat solutions that have small statistical uncertainty and are robust to outliers, we calculate a statistic, which we call $\sigma_{\rm jack}$, using star-flat fits to ten separate jackknife samples, each containing a randomly selected set of half the stars. The statistic, $\sigma_{\rm jack}$, is a measure of the variation in the star-flat solution across the samples.

We create a pixelated image of the best-fit star-flat model (in magnitudes) across the focal plane for each jackknife sample, where each pixel cell corresponds to an area of $20'' \times 20''$, or 100×100 CCD pixels. Each jackknife correction map can then be represented by A_{ij}^n, where i and j are the pixel coordinates, n denotes the nth jackknife sample, and A_{ij}^n is the mean of the star-flat model within pixel (i, j). We use the A_{ij}^n maps to assess the uncertainty of the star-flat fits. Since we are interested only in the relative spatially varying corrections, we subtract the median correction across the image from the correction in each pixel: $\delta A_{ij}^n = A_{ij}^n - {\rm median}(A^n)$. We then calculate the standard deviation $\sigma(\delta A_{ij})$ for each pixel across the jackknife fits.

To assess the uncertainty of the correction calculated from each star flat, we use the median of $\sigma(\delta A_{ij})$ across all pixels in the image, which we call $\sigma_{\rm jack}$.

3.4.5 Required Value of $\sigma_{\rm jack}$

Selecting a maximum acceptable value for $\sigma_{\rm jack}$ presents a tradeoff between two objectives. On the one hand, we want to measure the star flat for as many observing runs and pointings as possible to correct for any variation with position in the sky and with time. On the other hand, we want to apply a correction only when the statistical uncertainty on the correction is small. We adopted the criteria outlined in the following paragraph but, as shown in Table 1, the average values of the $\sigma_{\rm jack}$ statistic for each chip configuration are substantially better than these thresholds.

For chip configurations 8 and 9 (see Section 3.1), the *minimal* requirement for using the star-flat correction is that $\sigma_{\rm jack} < 0.03$ mag (i.e., star flat constrainted to ≈ 0.03 mag). For chip configurations 10_1, 10_2, and 10_3, where greater numbers of objects are generally available, we consider a fit acceptable if $\sigma_{\rm jack} < 0.01$ mag. We attempted star-flat fits to 471 sets, and 183 of the solutions satisfied these requirements.

A star-flat solution may be too poorly constrainted to meet the minimal $\sigma_{\rm jack}$ requirement for several reasons. These include low stellar density in the galaxy cluster field, exposures taken without camera rotation, no overlap with the SDSS footprint, and minimal telescope dithers between exposures. When the star-flat fit does not meet the $\sigma_{\rm jack}$ criterion, we look for a satisfactory star flat for a different filter of the same field and use the corrected $m_{\rm star}^{\rm model}$ magnitudes as reference $m_{\rm star}^{\rm cat}$ magnitudes. When even these additional

Table 1. Diagnostic fit statistics averaged across acceptable star flats, sorted by chip configuration and whether SDSS stellar photometry was available for at least 400 matched stellar objects. The statistic $\langle\sigma_{\rm jack}\rangle$ shows that the star-flat correction is well constrained.

Chip Configuration	SDSS Matches	Cluster/Filter/Run Combinations	$\langle\sigma_{\rm jack}\rangle$
10_3	None	3	0.003 mag
10_3	Yes	4	0.003 mag
10_1 & 10_2	None	69	0.004 mag
10_1 & 10_2	Yes	96	0.003 mag
8 & 9	None	6	0.009 mag
8 & 9	Yes	5	0.021 mag

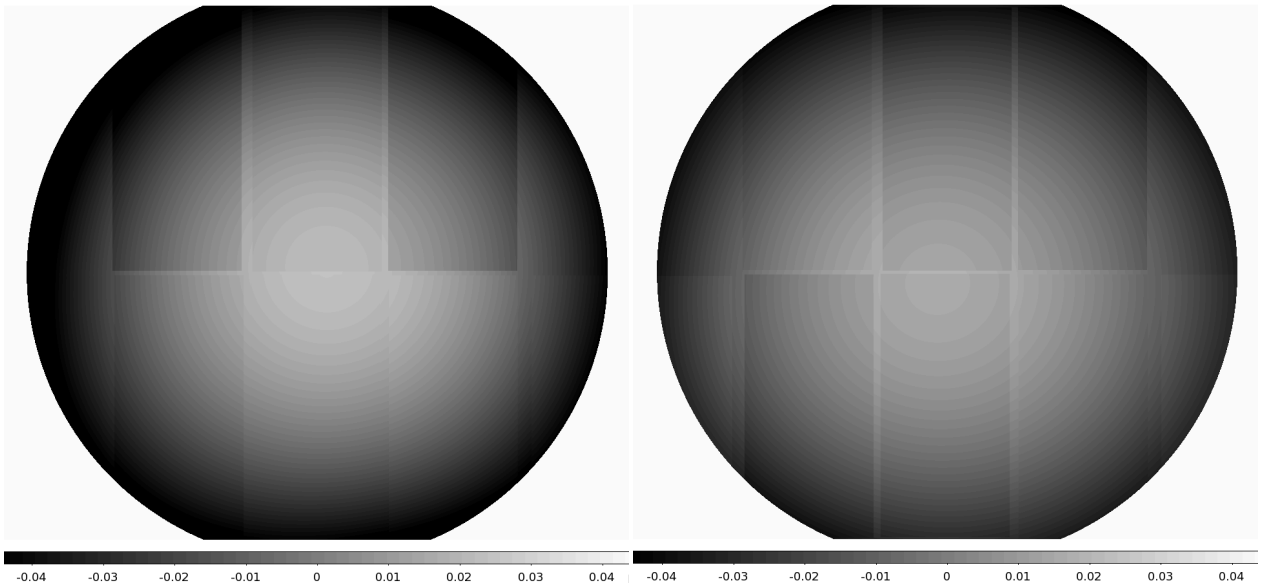

Figure 1. The average star-flat model for the Subaru SuprimeCam B_J (left panel) and R_C (right panel) filters. The star-flat models show our estimate of the average, position-dependent zeropoint correction to stellar magnitudes measured from images corrected with a night-sky flat (the 'superflat'). The best-fit star-flat model maximizes the agreement among flux measurements of the same stars in multiple positions, as well as agreement with available magnitudes from photometrically consistent catalogs (i.e., from the SDSS or previously corrected SuprimeCam or MegaPrime photometry). Dividing pixelated images (already corrected by the night-sky flat) by the star flat yields corrected images with uniform photometry. The shaded horizontal bar below each figure shows the correction to the night-sky flat field in magnitudes. We restrict photometry and star-flat fits to the area within 15′ of the center of the field because of increased levels of light scattered from outside the field of view into the periphery, strong vignetting, and changes in the point spread function at large radii. The model for the star flat consists of the product of third-order Chebyshev polynomials in x and y plus a chip-dependent offset, as described in Sec. 3.4.2.

constraints from $m^{\rm cat}_{\rm star}$ do not yield an acceptable solution, we correct the data by the satisfactory star flat for data taken closest in time (with the same filter and chip configuration).

3.5 The Measured Star-Flat Correction

Figure 1 shows the star-flat shape for the B_J and R_C bands, averaged across the fits that meet the $\sigma_{\rm jack}$ criteria for each band. The star-flat corrections averaged over satisfactory fits show a maximal variation across the 15′-radius field of ∼0.06 mag in the B_J and z^+ bands and ∼0.05 mag for V_J, R_C, and I_C. Within a 13′-radius field, the relative corrections are ∼0.05 mag for B_J and z^+ and ∼0.03-0.04 mag for V_J, R_C, and I_C. Figure 2 shows how the star-flat correction improves the agreement between the SuprimeCam V_J and SDSS magnitudes for the RXJ1720.1+2638 field.

3.6 Comparison with Capak et al. (2007) SuprimeCam Star Flat Analysis

To be able to extract accurate photometry for the COSMOS project, Capak et al. (2007) measured a star flat for Subaru SuprimeCam imaging taken from 2004 through 2005 (chip configuration 10_2). Before fitting for the star flat, Capak et al. (2007) first normalized images by a dome flat and then divided the dome-flat–normalized photometry by the Jacobian of the astrometric solution to explicitly correct for geometric distortion (∼3% at a radius of 13′). By contrast, we divided dome- or twilight-flat–normalized images by a night-sky flat, which shows variation of ∼0.005 mag between field center and 15′, and made no explicit correction for pixel size changes.

The COSMOS correction, including the ∼3% explicit adjustment for pixel size, agrees with our corrections to ∼(1-2)% within 13′ of the center of the field. The only difference with the COSMOS total correction that we find is that the B_J and z^+ corrections may be ∼1% greater than one would expect from only the geometric effect within 13′.

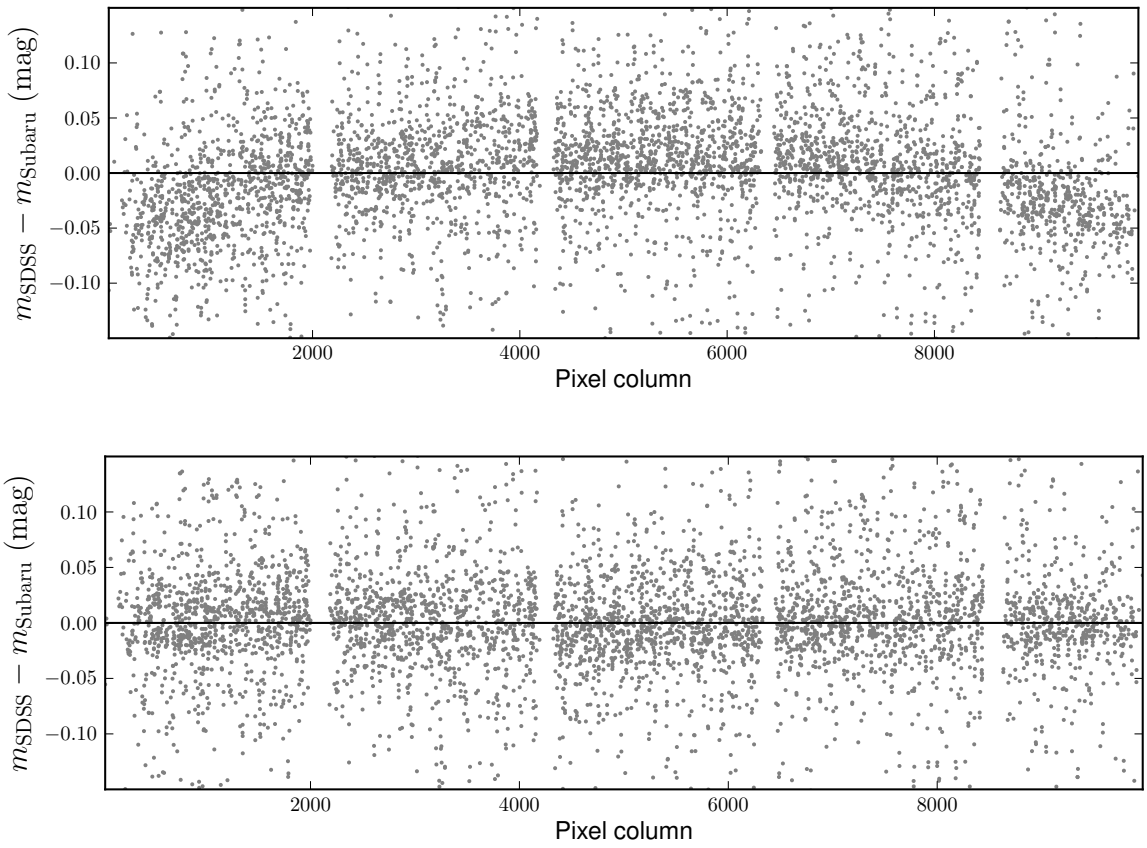

Figure 2. *Star*-flat correction removes strong spatial zeropoint variation that remains after *night sky*-flat correction. The top panel shows the comparison between SuprimeCam V_J instrumental magnitudes (extracted from *sky*-flat corrected images) and uniform SDSS stellar photometry in the RXJ1720.1+2638 galaxy cluster field, while the bottom shows the improved agreement after star-flat correction. A first-order color term is used to transform SDSS g' magnitudes to expected SuprimeCam V_J magnitudes. Flux measurements of the same stars at multiple positions on the focal plane, in particular before and after 90° camera rotations, place the strongest constraints on the star-flat model, except when fields have high stellar density and comparison magnitudes from photometrically consistent catalogs are available. Comparison SDSS magnitudes are important for constraining linear terms in the Chebyshev polynomials. (Without SDSS photometry of the field, linear terms are degenerate with variations in the zeropoint offsets between dithered exposures; in those cases, we exclude first-order terms from the Chebyshev polynomials.)

Since the images we analyze were taken between 2000 and 2009, and span three major SuprimeCam upgrades, we must characterize the star-flat corrections across all configurations. Chip-dependent zeropoints are substantially larger for data taken during the early 8- and 9-chip SuprimeCam configurations because the array included chips from different manufacturers.

3.7 Implementing Correct SWarp Image Resampling

Resampling the exposures of each cluster field taken using different camera rotations, in separate dithered positions, and multiple filters to a common pixel grid and coordinate system makes it possible to measure the magnitudes and colors of objects easily. As described earlier, geometric distortions through the optical paths of most wide-field telescopes yield a pixel scale (arcsecond pixel^{-1}) that decreases with increasing distance from the field center.

We find that the commonly used SWarp program (Bertin et al. 2002, version 2.19.1) requires a patch to its source code to preserve relative fluxes of point sources imaged by separate CCD sensors. The SWarp 'VARIABLE' FSCALASTRO_TYPE setting (in contrast to 'NONE' and 'FIXED') preserves the flux ratios of sources on the same CCD sensor during resampling, but we find that the ratios among the fluxes of objects on *different* CCD sensors become altered.

This problem arises from the fact that, in the SWarp source code, the pixel flux is multiplied by a factor that depends on the average pixel scale of each resampled image in the 'VARIABLE' FSCALASTRO_TYPE. This chip-dependent factor yields chip-dependent zeropoint offsets with the current SWarp version. A simple modification to the SWarp source code can repair this problem by removing the unneeded factor for each chip.

We discovered the problem with SWarp after all images were coadded, so we applied the appropriate position-dependent flux correction to the photometry of objects measured from resampled exposures.

4 USING STELLAR LOCUS MATCHING AS A CALIBRATION TOOL

The traditional approaches to calibrating photometry through standard-star observations or from overlap with well-calibrated surveys (e.g., SDSS) are not practical or sufficiently reliable for our

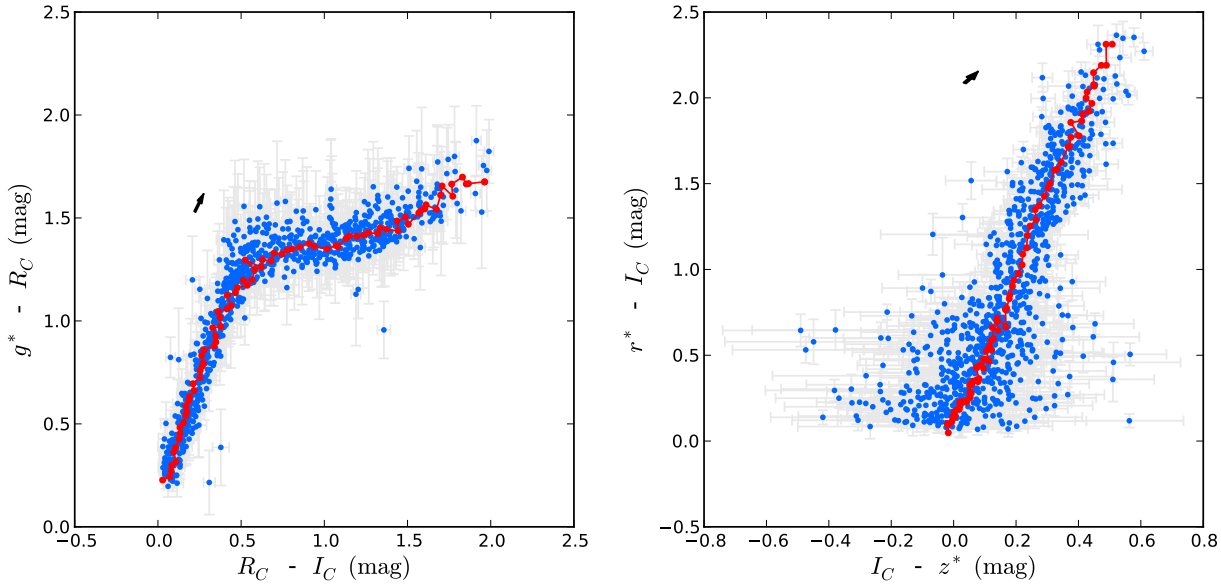

Figure 3. Color calibration of photometry through nine Subaru SuprimeCam ($B_J V_J R_C I_C z^+$) and CFHT MegaPrime ($g^* r^* i^* z^*$) filter bands of the RXJ1347-11 galaxy cluster field. We *simultaneously* vary eight zeropoints and hold one constant (here R_C) during the fit to maximize agreement between the instrumental stellar locus and the model (dereddened) stellar locus. The red points and lines show the model for the dereddened stellar locus in color-color space, and the blue points show the colors for the individual stars in the field after applying the best-fit photometric zeropoints. For each point along the SDSS $u'g'r'i'z'$ stellar locus (indexed by $g' - i'$ color), we construct a best-fit model spectrum that can reproduce the point's color (see Figure 4). To calibrate photometry, we compute synthetic magnitudes from each model spectrum and the total response functions of the filters and instrument used. These synthetic magnitudes form the model stellar locus that we use in each fit for unknown zeropoints shown. The arrow shows, for reference, the direction and magnitude of reddening due to dust predicted by the Schlegel et al. (1998) dust extinction map.

analysis of SuprimeCam and MegaPrime imaging. A substantial fraction of nights have no standard-star observations and, even when they are available, robust calibration is possible only in the most favorable atmospheric conditions. Bright SDSS stars ($R_C \lesssim$ 19 mag) saturate in our exposures, and Sloan coverage is therefore not useful for high precision calibration. To fit for accurate zeropoints, we apply an improved stellar locus matching method.

Investigations at several wavelengths show that the Galactic dust sheet extends only ~50-100 pc from the midplane (Drimmel & Spergel 2001; Marshall et al. 2006; Kalberla & Kerp 2009; Jones et al. 2011), and the vast majority of stars visible in SDSS, Subaru, and CFHT imaging are at distances beyond the edge of the Galactic dust sheet (e.g., High et al. 2009). Star colors lie predominantly in a narrow band in color-color space, called the stellar locus. The locus has only modest sensitivity to metallicity variations among Milky Way stars at wavelengths redder than ~5000 Å (Ivezić et al. 2007; High et al. 2009). Therefore, by shifting zeropoints for each band until the measured stellar locus matches the dereddened SDSS stellar locus, we can establish a photometric calibration that includes a correction for the Galactic dust.

As an example of a typical stellar locus and our model, we show in Figure 3 the results of a fit for the instrumental zeropoints of nine SuprimeCam and MegaPrime bands for the RXJ1347-11 galaxy-cluster field. Below, we discuss significant improvements to the zeropoint accuracy of stellar locus matching that can be achieved by first dereddening the measured SDSS stellar locus, then constructing a spectroscopic model for the dereddened locus, and finally solving for consistent zeropoints in multiple bands simultaneously (e.g., $B_J V_J R_C I_C z^+$). In the following section, we first review the astrophysical basis for using the stellar locus as a calibration tool and then describe our improved technique.

4.1 Stellar Populations Along the Locus

Several teams have used the stellar locus as a tool to calibrate optical photometry (MacDonald et al. 2004; Ivezić et al. 2004; High et al. 2009; Gilbank et al. 2011; Coupon et al. 2012). Recently, High et al. (2009) applied the calibration technique to $g'r'i'z'$ Magellan imaging of 11 galaxy clusters. For these $z < 0.25$ galaxy clusters, they fit the average color of the cluster red-sequence galaxies and estimated the cluster redshifts with 0.6% accuracy in $\sigma((z_p - z_s)/(1 + z_s))$ (see also High et al. 2010). To understand the effectiveness of the stellar locus technique as well as its limitations, they also scrutinized the astrophysical understanding of the Milky Way stellar locus. Here we discuss the constituents of the locus, their distances from the Earth, and the effect of metallicity variation in the Milky Way.

Blue stars are generally visible to much greater distances than red stars, because blue stars are predominately more luminous. As shown in Figure 3, the path of the locus of stars shows a sharp change in direction in the plot of $g^* - R_C$ versus $R_C - I_C$ at $R_C - I_C \approx 0.6$ (or SDSS $r' - i' \approx 0.7$). The part of the locus to the blue side of the kink includes A through K stars (members of the halo and disk main sequence), as well as an evolved halo population (High et al. 2009). The origin of the 'kink' is the fact that the disk-metallicity M-dwarf stars redward of the kink have substantially nonthermal spectra due to absorption by oxides and metal hydrides, including TiO, VO, CaH, and FeH (e.g., High et al. 2009; West et al. 2011). By contrast, low-metallicity M dwarfs have thermal

spectra, and their colors place them along an extrapolation of the locus to the blue side of $R_C - I_C \approx 0.6$. The absence of such a second branch in the stellar color-color plots for the Subaru and CFHT images analyzed here suggests that we detect few halo M dwarfs in our exposures. This absence is consistent with the faint intrinsic luminosities of M dwarfs ($10 < r < 15$ mag). SDSS identified only a few thousand M subdwarfs with high confidence across the entire SDSS footprint to their 22-mag limit in the r' band (LSST Science Collaborations et al. 2009).

4.2 Sensitivity of Stellar Colors to Metallicity

The stellar populations with useful photometry in an astronomical image will depend, at the bright end, on the exposure's saturation limit and, at the faint end, on the detection limit. Our SuprimeCam imaging generally saturates at $R_C \approx 19$ mag and yields detections to $R_C \approx 26$ mag. For SDSS exposures, the range of useful magnitudes in r' is between ∼14 and ∼22.5 mag.

Catalogs made from deeper exposures will include a higher fraction of halo members in the stellar locus to the blue side of the kink in the color-color plot in Figure 3(a). Although stars with $0.2 < g - r < 0.4$ are approximately evenly split between the disk and halo populations at SDSS depths, our Subaru and CFHT catalogs contain a higher fraction of halo stars, given the deeper limiting magnitudes. Since we use the SDSS stellar locus as a model for the locus in our deeper Subaru and CFHT exposures, we need to consider whether the properties of the stellar locus may change with a larger population of halo-metallicity main sequence stars.

Using SDSS photometry and spectroscopy, Ivezić et al. (2008) find that the halo population has a Gaussian metallicity distribution with mean $[\mathrm{Fe/H}]_{\mathrm{halo}} \approx -1.5$, while the metallicity of disk stars decreases with distance Z from the midplane according to $[\mathrm{Fe/H}]_{\mathrm{disk}} = (-0.78 + 0.35, \exp(-|Z|, \mathrm{kpc}^{-1}))$ dex.

High et al. (2009) use model stellar atmospheres to study how the metallicity difference between the disk and halo main sequence populations affects the color of their stellar population. They assign a metallicity of [Fe/H]= −0.5 for the disk population and a metallicity of [Fe/H]= −1.5 for the halo population. The difference in $g' - r'$ color for main sequence stars in the two populations, in the region of the stellar locus to the blue end of the kink, is only ∼0.01 mag. However, the $u' - g'$ colors for the disk main sequence stars are ∼0.1 mag redder than those for their halo counterparts.

For this reason, we elect not to use the stellar locus to calibrate near-UV bands for our 'Weighing the Giants' study of Subaru and CFHT imaging. Near-UV emission of stars has comparatively strong sensitivity to the difference between halo and disk metallicities (High et al. 2009), and the SDSS u'-band filter leak near 7100 Å additionally affects measurements of the stellar locus in colors that include the u' band. There are, however, strategies that may enable use of the stellar locus measured from SDSS magnitudes to calibrate near-UV photometry in future efforts.

4.3 SDSS Stellar Locus Corrected for Extinction

We measure the stellar locus from SDSS Data Release 8 (Aihara et al. 2011) photometry corrected for Galactic dust extinction. Stars are drawn from fields with comparatively low Galactic extinction ($A_V < 0.2$ mag) and their magnitudes corrected by the Schlegel et al. (1998) extinction map. We place stars into bins according to their $g' - i'$ color (a proxy for effective temperature) and, for a series of colors (e.g., $g' - r'$, $r' - i'$), measure the median stellar color within each bin following the general approach used by Covey et al. (2007).

High et al. (2009) instead used the Covey et al. (2007) stellar locus, which is not corrected for extinction by Milky Way dust. We find that $g' - z'$ locus color and photometric calibration change by ∼0.05 mag after correcting the stellar locus for Milky Way extinction.

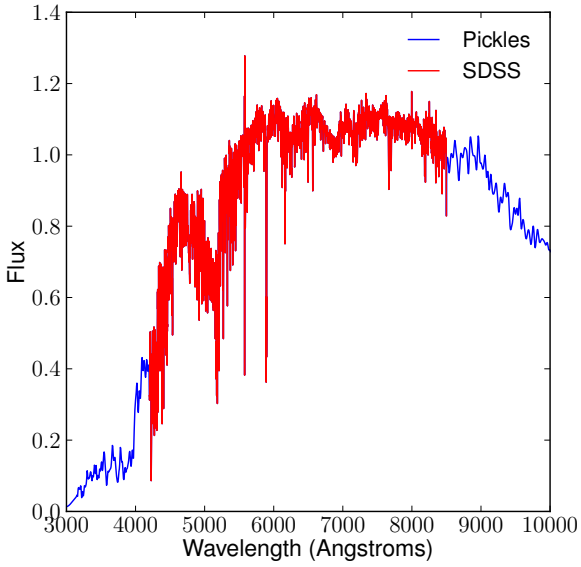

(a)

Figure 4. Best-fit stellar spectrum model for a sample point along the SDSS stellar locus: $g' - i' \approx 1.6$ mag. The red curve in the middle region shows the SDSS spectroscopic data for a K5 main sequence dwarf whose color best matches the color of this point on the stellar locus. The range of wavelengths covered by SDSS spectra (from 3900 to 9100 Å) must be extended in the blue and red regions to cover the Subaru/SuprimeCam and CFHT/Megaprime bandpasses that we wish to calibrate. The curves shown in blue correspond to the spectrum from the Pickles (1998) library with a shape most similar to the SDSS spectrum in the overlap region. These are multiplied by functions that are linear in wavelength to reproduce the full $u'g'r'i'z'$ color of the point on the stellar locus, as described in the text.

4.4 Defining Model Spectra Along the Locus

The broadband filters used for the Subaru and CFHT observations, especially the SuprimeCam $B_J V_J R_C I_C$ bandpasses, have substantially different transmission functions than SDSS $u'g'r'i'z'$ filters. The color transformations are nonlinear, and we found that a simple, linear color term yielded poor zeropoint solutions. To perform improved color transformations between magnitudes in different filter sets, we construct a comprehensive spectroscopic model for the SDSS stellar locus. An advantage of this spectroscopic model is that the locus for any filter system can be easily computed, requiring only the total response function for each filter. The total response function is the product of the transmission function for the atmosphere, reflectivity of the telescope mirrors, transmission function for the optics and filter, and the CCD-sensor wavelength-dependent response.

For each of 75 points along the SDSS locus, indexed by $g' - i'$ color, we identify the SDSS stellar spectrum (from spectroscopic data) whose synthetic $g'r'i'$ colors (i.e., $g' - r'$, $r' - i'$, and $g' - i'$)

best match the $g'r'i'$ colors for this point on the stellar locus. For this step, we use the CasJobs[2] tool to query the SDSS database. The wavelength range covered by SDSS spectra (3900 - 9100 Å) does not extend through the u' and z' bands, so we identify the Pickles (1998) main sequence dwarf stellar spectrum that best cross-correlates with the SDSS spectrum in the range of overlapping wavelengths. With the Pickles (1998) spectrum, we extend the SDSS spectrum at both the blue and red end. Figure 4 shows an example composite spectrum, constructed from SDSS and Pickles (1998) K5 main sequence dwarf spectra, for a stellar locus point with $g' - r' \approx 1.1$ mag and $r' - i' \approx 0.4$ mag.

We assemble a continuous spectrum by scaling the Pickles (1998) blue and red segments separately to match the SDSS spectrum in the overlapping wavelength ranges of 4100 to 4600 Å and 8000 to 9000 Å, respectively. The spliced spectrum is then comprised of the Pickles (1998) blue segment up to 4200 Å, the SDSS segment between 4200 Å and 8500 Å, and the Pickles (1998) red segment above 8500 Å, as can be seen in Figure 4. We next introduce functions that are linear in wavelength that allow us to adjust the Pickles (1998) segments to reproduce the locus point's $u'g'r'i'z'$ colors. We multiply the blue Pickles (1998) segment by a linear function, $F_{\rm blue}(\lambda) = A\lambda + B$, where $F_{\rm blue}(4200) = 1$, and then the red Pickles (1998) segment by a second linear function, $F_{\rm red}(\lambda)$, with $F_{\rm red}(8500) = 1$. We fit for the slope of each line to match the $u' - g'$ and $i' - z'$ colors, respectively, of the point on the stellar locus.

4.5 Fitting the Stellar Locus

The objective of our fitting algorithm is to find the set of zeropoints that yields the best match between the observed and model stellar locus. We perform a search for these zeropoints using χ^2 minimization and the downhill simplex method (Nelder & Mead 1965).

Calculating the χ^2 for a given model locus and set of filter zeropoints ZP_f is a two-step process. We follow a similar strategy to that of High et al. (2009) but employ an improved methodology that enables us to fit simultaneously and self-consistently for the complete set of unknown zeropoints.

For a given set of zeropoints ZP_f, we search, for each observed star, through all 75 points along the model locus to find the point with the best χ^2 (i.e., the best match to the observed stellar spectral energy distribution (SED)). Keeping the zeropoints fixed, we repeat this process for all stars, summing an overall χ^2 to calculate a goodness-of-fit (GOF) statistic. We repeat this overall process for each new set of zeropoints until the best set of zeropoints is found.

High et al. (2009) instead solved for the zeropoints of any two filters (e.g., ZP_g and ZP_i from $g-r$ and $r-i$ colors) by minimizing the weighted, perpendicular color-distance residual:

$$d^w_{\alpha\beta} = \frac{|\boldsymbol{d}_{\alpha\beta}|}{|\boldsymbol{\sigma}_\alpha \cdot \hat{d}_{\alpha\beta}|}, \tag{4}$$

where $\boldsymbol{\sigma}_\alpha$ is the vector of measurement errors, $\boldsymbol{d}_{\alpha\beta}$ is the vector distance in color space between star α and locus point β, and $\hat{d}_{\alpha\beta}$ is a unit vector with the same orientation as $\boldsymbol{d}_{\alpha\beta}$. Calculating distances in color space, however, becomes increasingly cumbersome for growing numbers of filters such as we have. In particular, n magnitude measurements produce $(n^2-n)/2$ colors (e.g., 10 colors for 5 bands, 15 colors for 6 bands) with correlated errors.

[2] http://casjobs.sdss.org/CasJobs/

To improve the accuracy of the calibration, we instead employ a simple χ^2 method that enables simultaneous fitting for large numbers of consistent zeropoints, and avoids correlated input errors that arise when calculating distances in color space. We follow several steps to measure the $\chi^2_{\rm tot}$ GOF for each set of ZP_f fit parameters. For each star α and locus point β, a common, relative zeropoint $O_{\alpha\beta}$ between $m_f^{\alpha(obs)}$ and $m_f^{\beta(model)} + ZP_f$ is shared across all filters f. This relative zeropoint $O_{\alpha\beta}$ accounts for the difference between the normalization of the star's instrumental magnitudes, which depends on the star's apparent magnitude, and the arbitrary normalization of the model SED. The $\chi^2_{\alpha\beta}$ agreement between $m_f^{\alpha(obs)}$ and $m_f^{\beta(model)} - ZP_f$ is a function of $O_{\alpha\beta}$:

$$\chi^2_{\alpha\beta}(O_{\alpha\beta}) = \sum_{f=1}^{n} \left(\frac{m_f^{\alpha(obs)} - (m_f^{\beta(model)} - ZP_f + O_{\alpha\beta})}{e_f^{\alpha(obs)}} \right)^2. \tag{5}$$

We identify the relative zeropoint $O_{\alpha\beta}$ that minimizes $\chi^2_{\alpha\beta}(O_{\alpha\beta})$ (i.e., maximizes the likelihood). This is simply the weighted mean of the differences between $m_f^{\alpha(obs)}$ and $m_f^{\beta(model)} - ZP_f$:

$$O^*_{\alpha\beta} = \frac{\sum_{f=1}^{n} (m_f^{\alpha(obs)} - (m_f^{\beta(model)} - ZP_f))/(e_f^{\alpha(obs)})^2}{\sum_{f=1}^{n} 1/(e_f^{\alpha(obs)})^2}. \tag{6}$$

For each star α, we loop over the locus points to find the locus point β with the smallest $\chi^2_{\alpha\beta}(O^*_{\alpha\beta})$ statistic, $\chi^{2,\rm min*}_{\alpha\beta}$. We then sum $\chi^{2,\rm min*}_{\alpha\beta}$ over all stars α to calculate the overall GOF statistic for the given set of input zeropoints ZP_f: $\chi^2_{\rm tot} = \sum_\alpha \chi^{2,\rm min*}_{\alpha\beta}$.

To find the best-fitting zeropoints, we use the amoeba downhill simplex method (Nelder & Mead 1965). We solve for zeropoints in all filters (except one) simultaneously. This yields more robust and accurate zeropoints than previous implementations and improves the accuracy of our photometric redshifts.

The open-source Python code is available at http://big-macs-calibrate.googlecode.com. Photometric calibration requires only a catalog of measured stellar magnitudes and the total transmission function for each filter.

4.6 Testing Stellar Locus Matching Against SDSS Calibration and SFD Dust Extinction

Of the 51 galaxy-cluster fields in the sample, 40 have available SDSS photometry. The galaxy-cluster fields in our sample span a wide range in RA and DEC (see Paper I), as well as Galactic latitude and longitude, and therefore the ranges of stellar metallicity and dust extinction are wide. We can use the available SDSS photometry to perform a consistency check on the spectroscopic locus model. We first correct the available SDSS stellar $g'r'i'z'$ photometry in each galaxy-cluster field by the Schlegel, Finkbeiner & Davis 1998 (SFD) extinction, and then perform stellar locus matching (SLM) on the corrected SDSS photometry. The residual color $(g'_{\rm SLM} - r'_{\rm SLM}) - (g'_{\rm SDSS} - r'_{\rm SDSS})$ has mean 0.006 mag and standard deviation 0.014 mag, while the residual color $(r'_{\rm SLM} - z'_{\rm SLM}) - (r'_{\rm SDSS} - z'_{\rm SDSS})$ has mean −0.005 mag and standard deviation 0.019 mag. This excellent agreement demonstrates the effectiveness of our stellar locus matching technique.

5 PHOTOMETRIC REDSHIFT ALGORITHMS AND TEMPLATES

We estimate photometric redshifts with the Bayesian BPZ code (Benítez 2000; Coe et al. 2006), which uses spectral templates

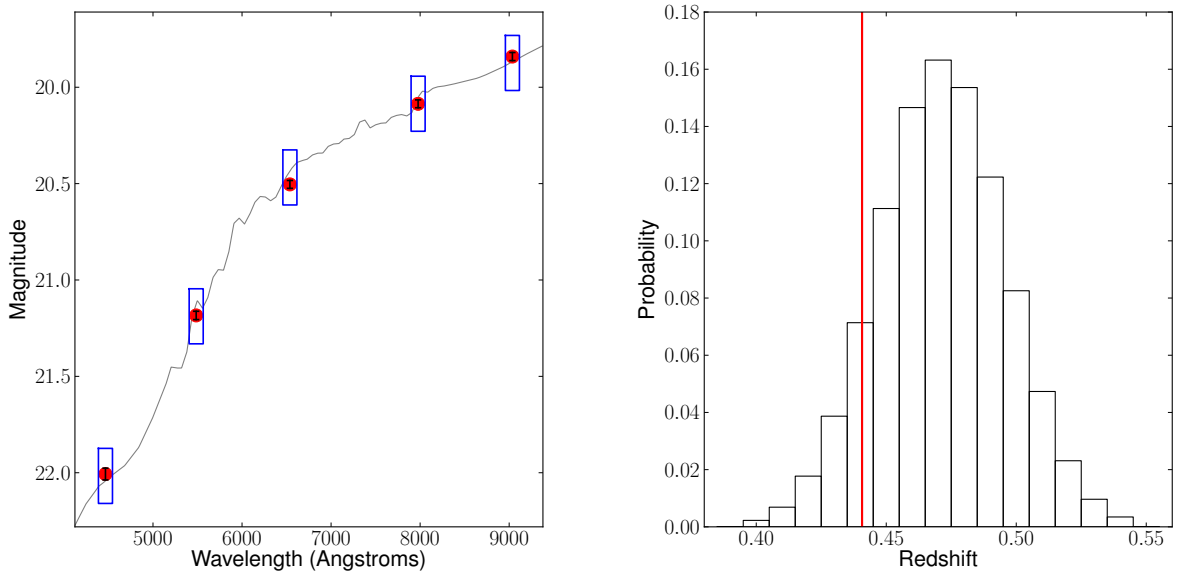

Figure 5. Best-fit SED model for a sample galaxy's broadband magnitudes from the BPZ photometric redshift code (left panel) and posterior redshift probability distribution (right panel). In this example, the template with greatest posterior probability is the elliptical galaxy spectrum from Coleman et al. (1980), modified by Capak (2004). The red points in the left panel show, in order of increasing central wavelength, the calibrated galaxy magnitude measured for the SuprimeCam B_J, V_J, R_C, I_C, and z^+ bands. The blue rectangles show the expected flux for the elliptical SED in these photometric bands. In the right panel, the horizontal coordinate of the vertical red line is the spectroscopic redshift of this elliptical galaxy.

as a model for the rest-frame SEDs of galaxies. Constraining the possible redshifts of galaxies based on their broadband colors (Baum 1962) is feasible because of regular features (e.g., the 4000 Å break) in rest-frame galaxy spectra. Given galaxy photometry in n broadband filters, the BPZ code defines $n-1$ colors $C = \{c_f\}$ relative to a 'base' filter (e.g., the band in which the galaxies were selected). BPZ computes the likelihood $p(C|z, T)$ of the observed galaxy colors C at a discrete series of possible redshifts z (e.g., 0.01, 0.02, 0.03, ...) for each galaxy template T.

Benítez (2000) introduced the use of prior probability density functions $p(z, m, T)$ into galaxy photometric redshift estimation, which depend on galaxy redshift z, apparent magnitude m, and template type T. He calibrated the parameters of these prior functions using 737 galaxies, including ~130 with spectroscopic redshifts, with $20 < I < 27$ from the HDFN (Williams et al. 1996), and 591 additional galaxies with spectroscopic redshifts and $20 < I < 22.5$ from the Canada-France Redshift Survey catalog (Lilly et al. 1995) with spectral classification from $V-I$ colors. When the colors C are consistent with the SED templates at multiple redshifts, the prior function can alleviate or break redshift degeneracies. Here we use the Benítez (2000) prior functions with a modest adjustment that increases the probability at low redshift ($z < 0.2$; see Erben et al. 2009). The posterior redshift probability distribution is

$$p(z) \equiv p(z|C, m) \propto \sum_T p(C|z, T)p(z, m, T). \quad (7)$$

The posterior probability $p(z)$ distribution is then smoothed, using the BPZ code, with a Gaussian that we specify to have $\sigma(z/(1 + z))$=0.03.

5.1 Most Probable Redshift z_p

The peak of the posterior redshift probability distribution $p(z)$ is, by definition, the most probable redshift of the galaxy, z_p (the BPZ parameter BPZ_Z_B). We use BPZ to compute, from the estimated $p(z)$ distribution, the probability that the galaxy redshift is within $\pm 0.1(1+z_p)$ of z_p,

$$\mathrm{ODDS} = \int_{z_p-0.1(1+z_p)}^{z_p+0.1(1+z_p)} p(z)dz. \quad (8)$$

For example, the ODDS statistic for a Gaussian $p(z)$ centered at z_p with standard deviation $\sigma = 0.05(1 + z_p)$ would be 0.95.

5.2 Template Set

The performance of the BPZ code depends on the template library. For this study, we use the template set assembled by Capak (2004), which comprises elliptical, Sbc, Scd, and Im spectra from Coleman et al. (1980) and two starburst templates from Kinney et al. (1996). Capak (2004) adjusted these templates both to increase agreement between spectroscopically determined redshifts and the BPZ most probable redshift z_p and to match the colors of galaxies fainter than the limiting magnitudes of spectroscopic samples.

The Capak (2004) templates are ordered by type (see list above), and, before fitting, we generate additional templates by interpolating eight times between adjacent templates in this ordered list (i.e., INTER=8).

Figure 5 shows an example photometric redshift fit to a galaxy with $B_J V_J R_C I_C z^+$ magnitudes. We show the best-fit template and measured galaxy magnitudes, as well as the $p(z)$ distribution and spectroscopic redshift value.

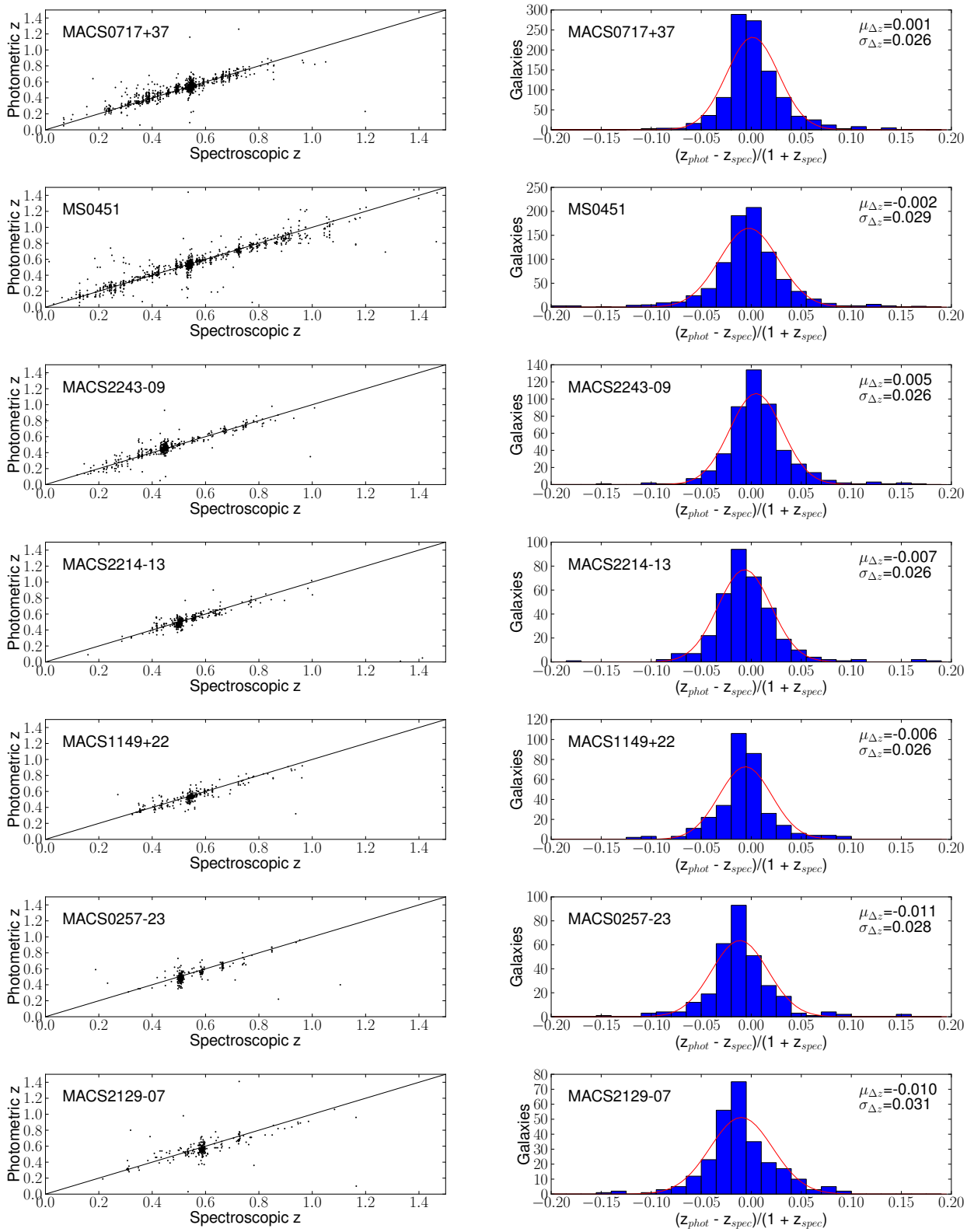

Figure 6. (Plots for seven clusters are shown on next page.) Left panels show the most probable photometric redshift z_p plotted against spectroscopic redshift z_s for galaxies in fourteen cluster fields with at least five bands of photometry. Spectroscopic redshifts are principally from Keck multi-fiber spectroscopy of cluster fields, with additional measurements collected from the NASA Extragalactic Database (NED). We show only photometric redshift estimates for galaxies for which the $p(z)$ probability distribution shows substantial weight close to the most probable redshift z_p (BPZ ODDS > 0.9). Right panels show histograms of $\Delta z = (z_p - z_s)/(1 + z_s)$; the overlaid curves (in red) and the statistics for the mean $\mu_{\Delta z}$ and standard deviation $\sigma_{\Delta z}$ correspond to Gaussian fits that exclude outliers with $|\Delta z| > 0.1$.

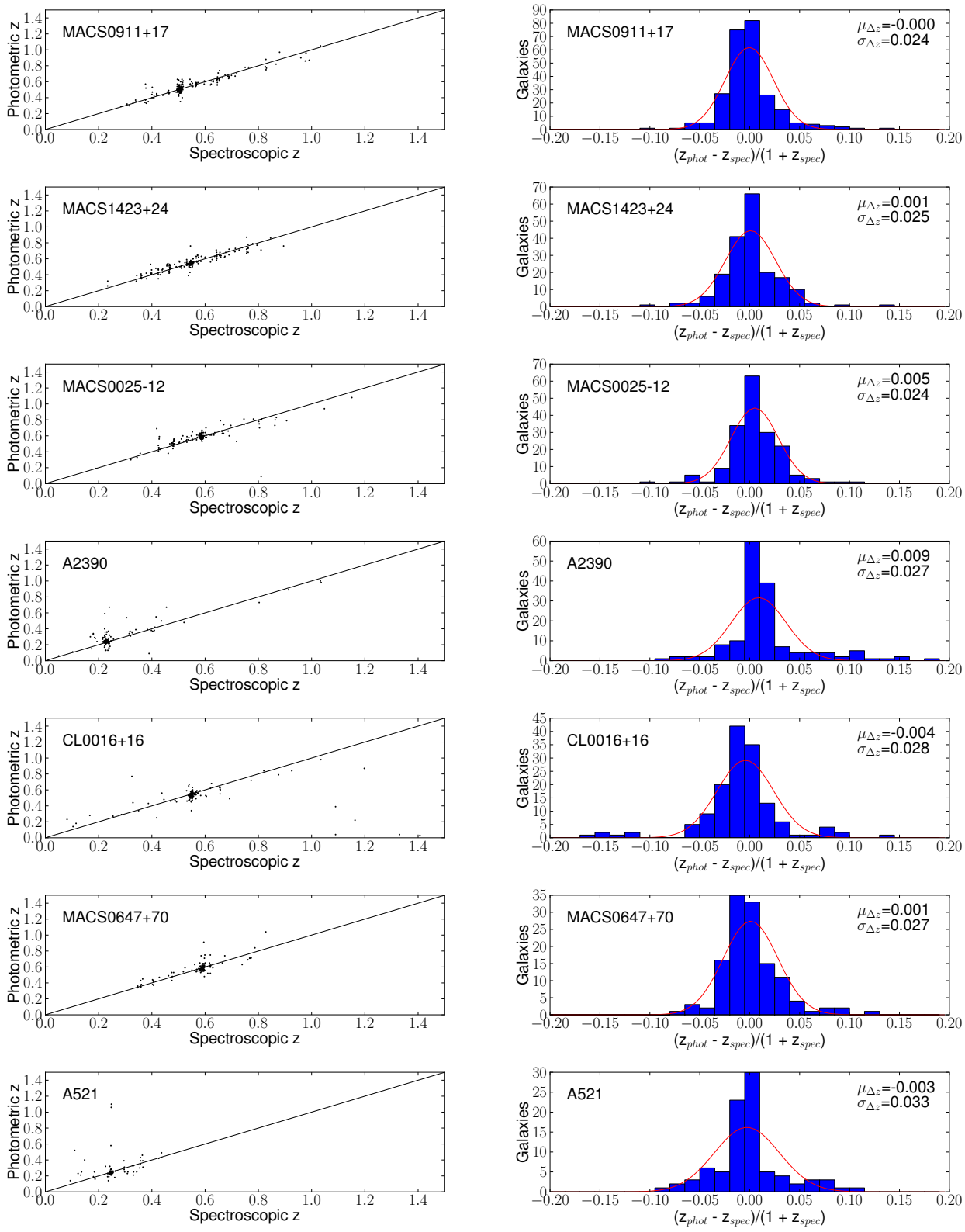

Figure 6 – *continued*

6 GALAXY SED EXTRAPOLATION TO FIND u^* AND B_J ZEROPOINTS

The photometric calibration of very blue filters, particularly u^*, from stellar locus matching is more challenging than for redder bands. Absorption by metals at near-UV and blue-optical wavelengths causes the u^* and B_J magnitudes of main sequence stars to depend more strongly on the chemical abundances in the stellar atmospheres than V_J, R_C, I_C, and z^+ magnitudes (see Section 4.2). Consequently, the stellar locus shows more variation across the sky in the u^* and B_J bands than in redder bandpasses.

We have therefore developed a technique to adjust Megaprime u^*-band and SuprimeCam B_J-band zeropoints after stellar locus matching calibration. We use the BPZ photometric redshift code to calculate for each galaxy the expected u^* and B_J magnitudes for each galaxy given the calibrated photometry at redder observer-frame wavelengths (e.g., V_J, R_C, I_C, and z^+), based on the best-fit SED template model (e.g., elliptical, Sbc) and redshift. Our method employs a training set of 10,000 galaxies, drawn randomly from the galaxies whose u^* and B_J magnitudes have uncertainties less than 0.05 mag. We modify the photometry catalog so that B_J magnitudes are assigned an uncertainty of 0.2 and every u^+ magnitude is assigned an uncertainty of 90 mag (effectively removing any constraint from u^+ magnitudes).

The zeropoint corrections for the u^* and B_J bands are estimated as the median difference $\mu_{1/2}$ between the predicted and measured magnitudes for galaxies,

$$ZP_{\rm new} - ZP_{\rm old} = \mu_{1/2}(m_{\rm gal}^{\rm BPZ} - m_{\rm gal}^{\rm exp}), \quad (9)$$

although the peak as opposed to median difference could possibly yield improved accuracy. After calculating photometric redshifts for the training set of galaxies, we then reject any galaxy with BPZ ODDS parameter less than 0.95 and most probable photometric redshift smaller than $z_p = 0.4$ so that the 4000 Å break does not fall near the u^* or B_J bandpasses. These criteria yield a sample of ~1000 training galaxies. We apply this technique to fields for which we have u^* or B_J observations in addition to observations in at least four other bandpasses.

The zeropoints we estimate with this technique will of course depend on the accuracy of the BPZ template set used to compute the expected u^* and B_J magnitudes. This procedure generally yields small ~0.01 mag adjustments to the B_J-band zeropoint calibrated through stellar locus matching. We do not use available u^*-band photometry for measuring cluster masses (Paper III).

7 PHOTOMETRIC CALIBRATION TESTS

We demonstrate the reliability of the stellar-locus-matching zeropoint calibration, as well as the performance of the redshift estimation, by comparing our estimates for the most probable photometric redshift z_p and the posterior probability distribution $p(z)$ to redshifts derived from spectra in both our galaxy cluster fields and the Cosmic Evolution Survey (COSMOS; Scoville et al. 2007) field, as well as accurate photometric redshifts from thirty-band photometry of COSMOS galaxies (COSMOS-30; Capak et al. 2007; Ilbert et al. 2009).

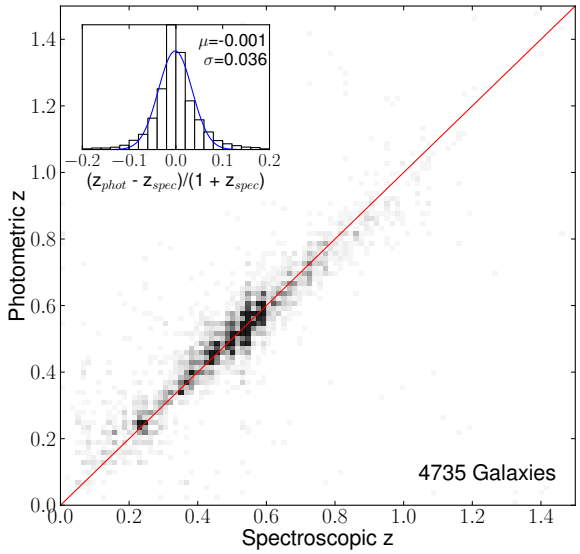

Figure 7. Most probable photometric redshift z_p plotted against spectroscopic redshift z_s for 4735 galaxies with BPZ ODDS > 0.9, in cluster fields with at least five bands of photometry. The grayscale intensity is proportional to the number of galaxies in each bin. Spectroscopic redshifts are from Keck, Gemini, and VLT spectroscopy of cluster fields, with additional measurements collected from the NASA Extragalactic Database. The histogram in the top left corner shows the distribution of $\Delta z = (z_p - z_s)/(1 + z_s)$; the overlaid curve (in blue) and the statistics for the mean μ and standard deviation σ correspond to Gaussian fits that exclude outliers with $|\Delta z| > 0.1$.

7.1 Spectroscopic Redshift Comparisons in the Cluster Fields

7.1.1 Galaxy Samples in Cluster Fields

We have measured, or compiled from the NASA Extragalactic Database[3], spectroscopic redshifts for 5007 galaxies in 27 cluster fields with five bands of photometry. We acquired spectra for galaxies in our cluster fields (e.g., Barrett 2006; Ma et al. 2008) with the Deep Imaging Multi-Object Spectrograph (DEIMOS) on the Keck-II telescope, the Low Resolution Image Spectrometer (LRIS) on Keck-I, the Gemini Multi-Object Spectrographs (GMOS) on the Gemini telescope, and the Visible Multi-Object Spectrograph (VIMOS) on the VLT. Of the 5007 galaxies, 4735 (95%) have BPZ ODDS > 0.9. In Figure 6, we plot the most probable photometric redshift z_p versus the spectroscopic redshift z_s for these galaxies with BPZ ODDS > 0.9 in the 14 cluster fields with the largest numbers of available spectroscopic redshifts. The photometric redshifts z_p for each of these 14 fields have typical accuracy of $\sigma((z_p - z_s)/(1 + z_s)) \lesssim 0.03$ and bias $(z_p - z_s)/(1 + z_s) \lesssim 0.01$, with $|(z_p - z_s)/(1 + z_s)| > 0.1$ outliers excluded.

7.1.2 Combined Sample of Galaxies in Cluster Fields

Figure 7 compares the most probable photometric redshift z_p to the spectroscopic redshift z_s for the combined sample of galaxies with spectroscopic redshifts and BPZ ODDS > 0.9, across all cluster fields. The photometric redshifts have accuracy of $\sigma((z_p - z_s)/(1 + z_s)) = 0.036$ and bias of

[3] http://ned.ipac.caltech.edu/

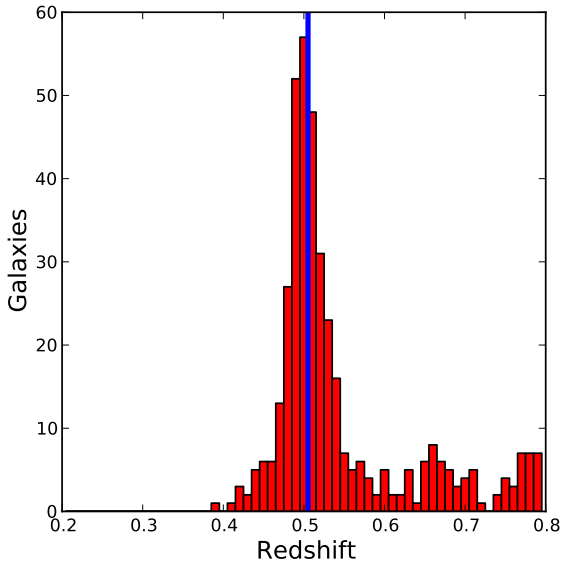

Figure 8. Histogram of the most probable photometric redshift z_p for members of the red sequence in MACS0911+17. The spectroscopic redshift of the cluster ($z_s = 0.51$) is shown as a blue vertical line. See Sec. 7.2 for details on the selection of red-sequence galaxies. These plots provide a diagnostic check of the photometric redshift quality available even when few spectroscopic redshifts are available.

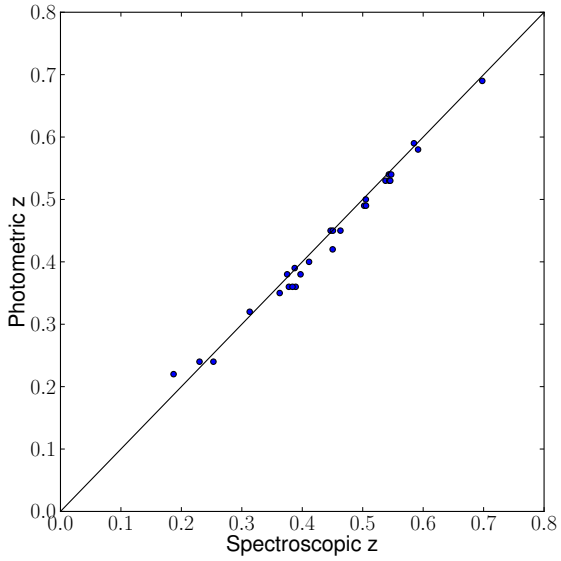

Figure 9. Peak photometric redshift $z_{\rm peak}$, for galaxies on the red sequence in each cluster field, plotted against the spectroscopic cluster redshift $z_{\rm cluster}$. The redshift estimate $z_{\rm peak}$ corresponds to the center of the z_p redshift bin (with bin width $\Delta z = 0.01$) with the greatest number of red sequence members. Figure 8 shows an example z_p histogram, for the MACS 0911+17 red sequence.

$\langle (z_p - z_s)/(1+z_s) \rangle = -0.001$, with $|z_p - z_s|/(1+z_s) > 0.1$ outliers (8.2% of galaxies) excluded.

The $\sigma((z_p - z_s)/(1+z_s)) = 0.036$ distribution is tighter than the $\sigma((z_p - z_s)/(1+z_s)) \approx 0.05$ that might be expected for galaxies with BPZ ODDS ≈ 0.95 (as defined in Section 5.1). A discrepancy, here as well as in comparisons that follow, can reasonably be attributed to the fact that the BPZ $p(z)$ distribution is smoothed with a $\sigma(z/(1+z))$=0.03 normal distribution before the ODDS parameter is calculated, and the fact that we reject $|(z_p - z_s)/(1+z_s)| > 0.1$ outliers when we compute $\sigma((z_p - z_s)/(1+z_s))$.

7.2 Photometric Redshifts of Galaxies on the Red Sequence

Using plots of galaxy color versus magnitude for each cluster field (e.g., $V_J - R_C$ versus V_J), we find the best-fit slope, intercept, and width of the distributions of red sequence galaxies for each cluster. We use these parameters to identify the galaxies along the red sequence (see Paper III for details). These samples may include foreground and background galaxy populations that happen to have the same colors and magnitudes as the red sequence – a contamination that becomes increasingly significant at fainter magnitudes. Figure 8 shows the histogram of most probable photometric redshifts z_p with BPZ ODDS > 0.90, for galaxies along the MACS0911+17 red sequence.

For cluster fields imaged through five or more filters (e.g., $B_J V_J R_C I_C z^+$), we plot in Figure 9 the peak redshift in the histogram of most probable redshifts, $z_{\rm peak}$, against the galaxy cluster spectroscopic redshift $z_{\rm cluster}$. While we have not otherwise made use of available near-UV photometry when computing photometric redshifts, we include CFHT MegaPrime u^* photometry to estimate $z_{\rm peak}$ for the lowest redshift cluster in the sample, Abell 383, since near-UV photometry, combined with blue optical photometry, bracket the 4000 Å break of $z < 0.2$ galaxies. The dispersion of $z_{\rm peak}$ is $\sigma((z_{\rm peak} - z_{\rm cluster})/(1+z_{\rm cluster})) = 0.011$ and the bias is $\langle (z_{\rm peak} - z_{\rm cluster})/(1+z_{\rm cluster}) \rangle = -0.005$. The histogram bins have $\Delta z = 0.01$ width, which places a lower limit on the accuracy of the cluster redshift estimates. A more accurate estimate of the peak cluster redshift could be obtained by applying, for example, a weighted Gaussian-kernel density estimator to interpolate between adjacent bins and by estimating photometric redshifts with greater precision than $\Delta z = 0.01$.

7.3 Galaxies in the COSMOS Survey

Accurate redshifts based on thirty-band photometry (Capak et al. 2007; Ilbert et al. 2009) are available for galaxies to $i^+ \approx 25$ mag in a 2 deg^2 field imaged for the Cosmic Evolution Survey (COSMOS; Scoville et al. 2007). Spectroscopic redshifts are also available for a sample of COSMOS galaxies with $I < 22.5$ mag (zCOSMOS; Lilly et al. 2009). The photometry of the COSMOS field includes SuprimeCam $B_J V_J r^+ i^+ z^+$ magnitudes, which we use to estimate photometric redshifts in an identical manner as for the photometry of the galaxy cluster fields, after recalibrating their zeropoints.

The magnitude limit of $i^+ \approx 25$ for the COSMOS catalog is comparable to that of our Subaru and CFHT galaxy cluster imaging, and beyond the completeness limit of today's spectroscopic samples. To test the five-filter photometric redshift estimates, we apply to the COSMOS-30 photometry catalog the same stellar locus matching and photometric redshift estimation procedure as we do for the cluster fields. We compare our most probable $B_J V_J r^+ i^+ z^+$ photometric redshifts z_p to zCOSMOS spectroscopic redshifts and COSMOS-30 photometric redshifts estimated from thirty broad, intermediate, and narrow bands spanning the UV to the mid-IR (Ilbert et al. 2009). The accurate COSMOS-30 photometric redshifts en-

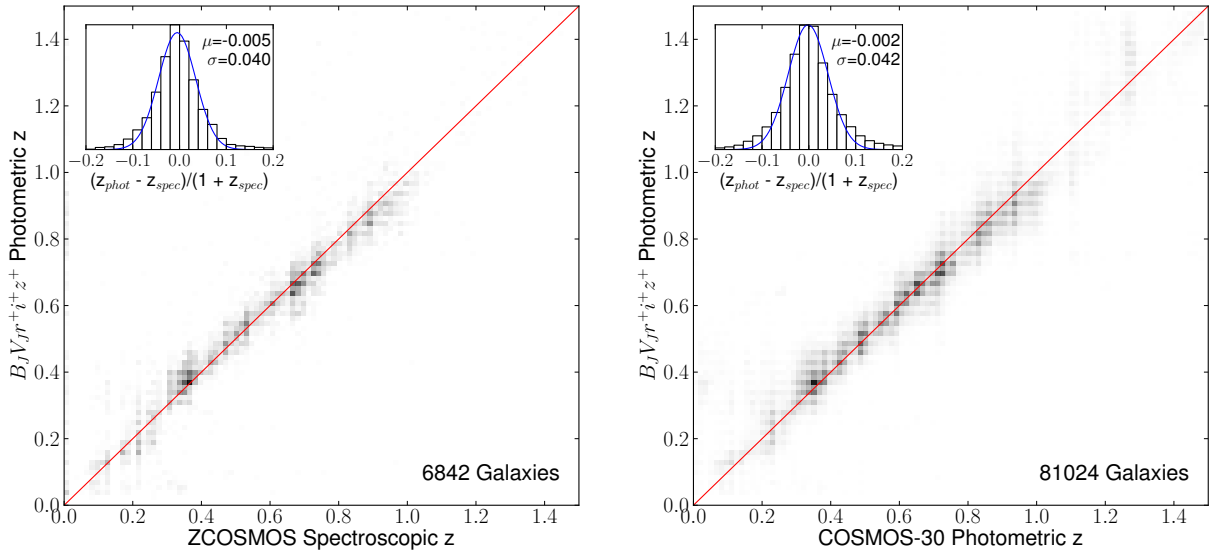

Figure 10. The left panel shows the most probable redshift z_p calculated from five Subaru bands ($B_J V_J r^+ i^+ z^+$) in the COSMOS catalog plotted against the zCOSMOS spectroscopic redshifts for 6842 galaxies. In the right panel, z_p is plotted against the COSMOS-30 photometric redshifts for 81,024 galaxies. The five-band z_p values are computed from the COSMOS photometry recalibrated using stellar locus matching. We include a galaxy in the plot only if BPZ ODDS > 0.9. The histogram in the top left corner of each plot shows the distribution of $\Delta z = (z_p - z_{\rm COSMOS})/(1 + z_{\rm COSMOS})$; the overlaid curve (in blue) and the statistics for the mean μ and standard deviation σ correspond to Gaussian fits that exclude outliers with $|\Delta z| > 0.1$.

able us to also test the posterior redshift probability distributions $p(z)$ based on five bands of photometry.

7.3.1 *zCOSMOS Spectrosopic Redshifts with $I < 22.5$*

Lilly et al. (2009) measured spectroscopic redshifts for galaxies in the COSMOS field and made publicly available the spectroscopic redshifts for targets with $I < 22.5$ (the zCOSMOS bright sample). The left panel of Figure 10 shows the most probable photometric redshift z_p based on $B_J V_J r^+ i^+ z^+$ photometry recalibrated with stellar locus matching for the COSMOS field versus the zCOSMOS spectroscopic redshifts z_s, for galaxies with BPZ ODDS > 0.9. The histogram in the upper left corner of the panel shows the level of agreement between z_p and z_s. The photometric redshifts have accuracy of $\sigma((z_p - z_s)/(1 + z_s)) = 0.040$ and bias of $\langle(z_p - z_s)/(1 + z_s)\rangle = -0.005$, with $|z_p - z_s|/(1 + z_s) > 0.1$ outliers (10.5% of galaxies) excluded. Only the galaxies with BPZ ODDS > 0.9 are plotted, which includes 6842 of 7959 galaxies.

7.3.2 *COSMOS-30 Photometric Redshifts of Galaxies with $i^+ < 25$*

Ilbert et al. (2009) estimated redshifts using the thirty-band photometry available in the COSMOS survey for several hundred thousand galaxies to $i^+ < 25$ mag (the COSMOS-30 redshifts). These authors used the LePhare code (Arnouts et al. 1999; Ilbert et al. 2006) and rest-frame galaxy templates that include narrow line features. The accuracy of COSMOS-30 photometric redshifts, estimated by comparing them to the zCOSMOS spectroscopic redshifts z_s for the faint sample, ranges from $\sigma((z_{\rm COSMOS-30} - z_s)/(1 + z_s))$=0.007 at $i^+ < 22.5$ mag to $\sigma((z_{\rm COSMOS-30} - z_s)/(1 + z_s))$=0.06 at $i^+ \approx 24$ mag.

The right panel of Figure 10 compares the most probable photometric redshift z_p we estimate from recalibrated COSMOS $B_J V_J r^+ i^+ z^+$ magnitudes to the COSMOS-30 photometric redshift. The photometric redshifts have a standard deviation of $\sigma((z_p - z_{\rm COSMOS-30})/(1 + z_{\rm COSMOS-30})) = 0.042$ and bias of $\langle(z_p - z_{\rm COSMOS-30})/(1 + z_{\rm COSMOS-30})\rangle = 0.002$, with $|(z_p - z_{\rm COSMOS-30})/(1 + z_{\rm COSMOS-30})| > 0.1$ outliers (14.2%) excluded. Only galaxies with BPZ ODDS > 0.9 are plotted, which includes 81,024 of 113,316 galaxies.

Representing the redshift probability distribution $p(z)$ for each galaxy as a single redshift (e.g., the most probable redshift z_p) neglects the sometimes substantial probability that the true galaxy redshift may have a very different value (e.g., Cunha et al. 2009; Abrahamse et al. 2011; Sheldon et al. 2011). Single-point estimates can lead to inaccurate conclusions, although the degree of inaccuracy will vary with the question being addressed and the precise $p(z)$ distribution. The $p(z)$ distributions for the majority of COSMOS galaxies with $B_J V_J r^+ i^+ z^+$ photometry to $i^+ \lesssim 25$ cannot be parameterized with a simple function (e.g., the sum of two Gaussian distributions).

The COSMOS data allow us to assess the accuracy of the $B_J V_J r^+ i^+ z^+$ posterior redshift probability distributions $p(z)$. We partition galaxies from the COSMOS-30 catalog into bins according to most probable redshift z_p, with bin widths of 0.2. For the galaxies in each redshift bin, we calculate the stacked $p(z)$ distribution $\sum_{gal} p(z)$ from our $B_J V_J r^+ i^+ z^+$ data. In Figure 11, we compare the stacked distribution from $B_J V_J r^+ i^+ z^+$ photometry to the redshift distribution for thirty-band Ilbert et al. (2009) COSMOS-30 photometric redshifts for galaxies with $i^+ < 25$ mag and with z_p in four redshift ranges. We include all galaxies with BPZ ODDS > 0.5. The comparisons show agreement between the $p(z)$ distribution we estimate and the Ilbert et al. (2009) COSMOS-30 estimate, which uses substantially more complete photometry.

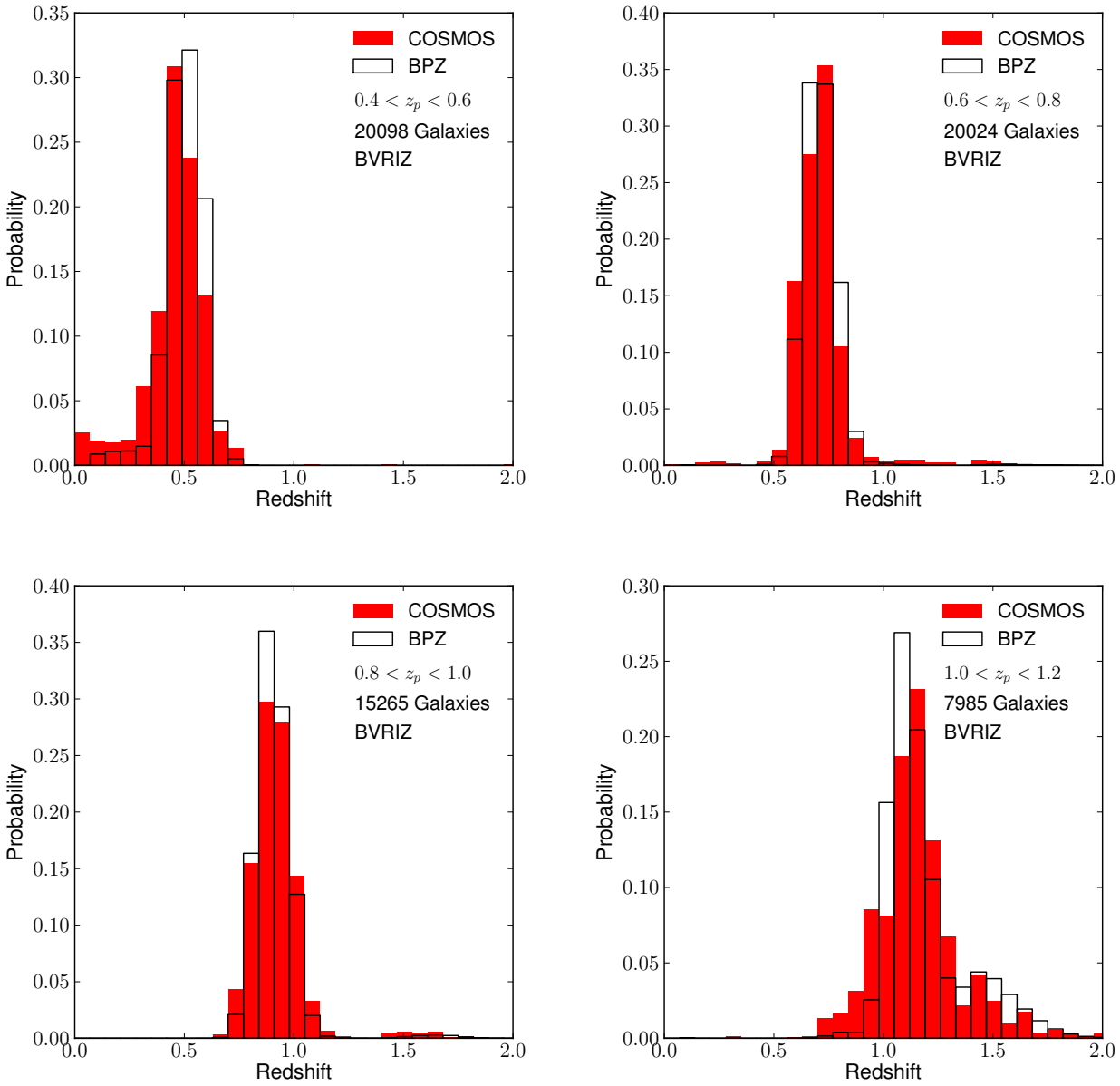

Figure 11. Stacked $p(z)$ distribution, $\sum_{gal} p(z)$, from $B_J V_J r^+ i^+ z^+$ photometry (open histogram) compared with the redshift distribution for thirty-band Ilbert et al. (2009) COSMOS-30 photometric redshifts (red histogram) for galaxies with $i^+ < 24.5$ mag and with z_p in four redshift ranges: $0.4 < z_p < 0.6$, $0.6 < z_p < 0.8$, $0.8 < z_p < 1$, and $1 < z_p < 1.2$. We include all galaxies with BPZ ODDS > 0.5. The comparisons show good agreement between the $p(z)$ distribution from our analysis and the Ilbert et al. (2009) estimates that use substantially more complete photometry. We use the more informative $p(z)$ distribution, rather than the most probable redshift z_p to measure galaxy-cluster masses. As discussed in Paper III, this leads to significantly improved accuracy in our weak-lensing mass results.

8 TOMOGRAPHIC WEAK LENSING

Correlations in the cosmic shear field hold significant promise as a tool for investigating dark energy (e.g., Hoekstra et al. 2006; Massey et al. 2007b; Fu et al. 2008; Schrabback et al. 2010). However, accessing the statistical power available from upcoming surveys (e.g., PanSTARRS, Dark Energy Survey, SkyMapper, Large Synoptic Sky Survey) to constrain cosmological parameters will require a complete characterization of the biases of both shear measurements and photometric redshift algorithms. The massive galaxy clusters in our sample provide ideal proving grounds for these techniques because the deep gravitational potentials of the galaxy clusters should yield strong tomographic shear signals.

The growth in shear with increasing redshift of a galaxy behind a gravitational lens (z_S) is sensitive to cosmological parameters through its dependence on the ratios of angular diameter distances (Jain & Taylor 2003; Taylor et al. 2007). The tangential shear at a radius r from the cluster center is given by

$$\gamma_t(r, z_S) = \frac{\overline{\Sigma}(< r) - \overline{\Sigma}(r)}{\Sigma_c}, \tag{10}$$

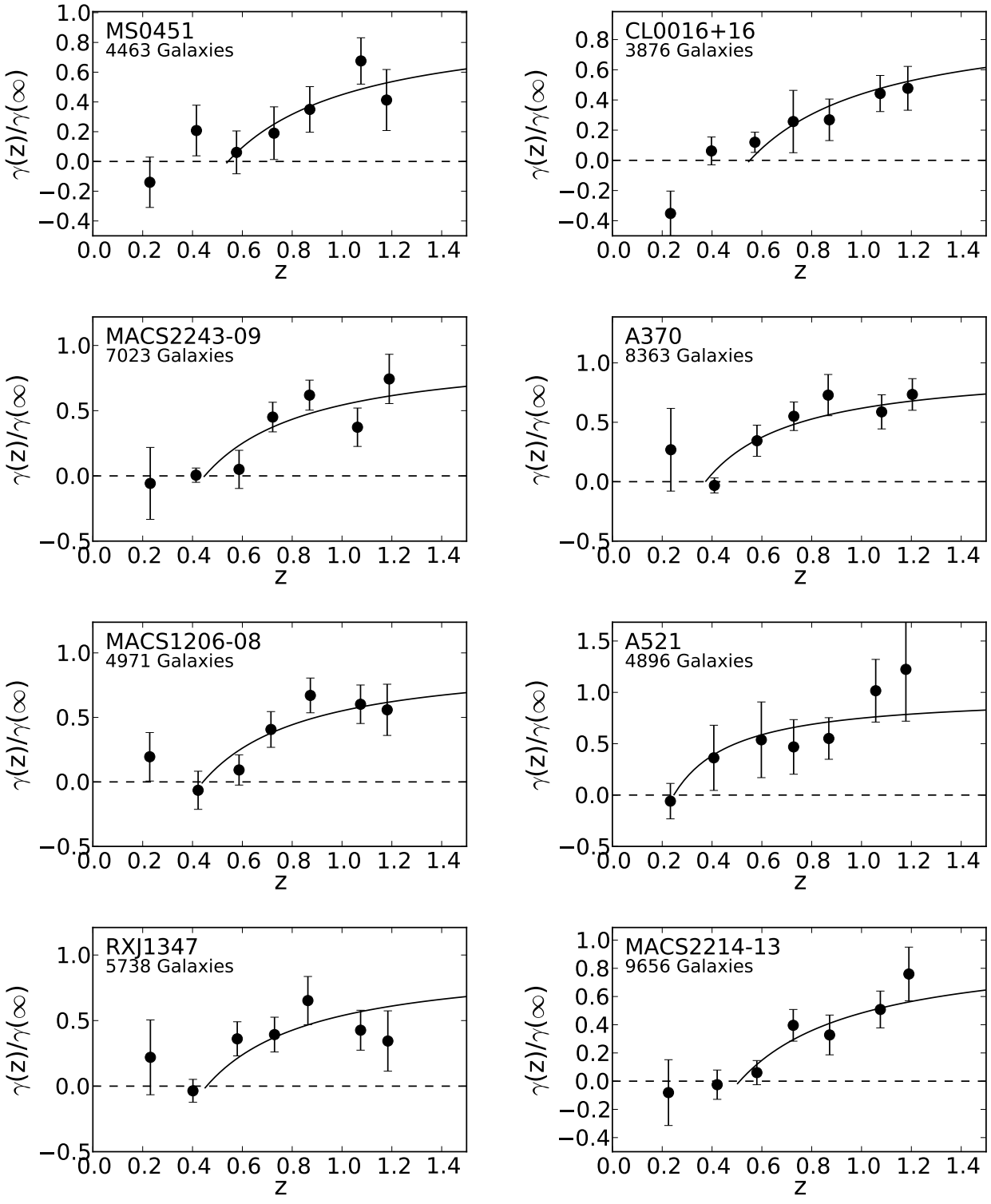

Figure 12. The measured weak-lensing shear as a function of most probable redshift z_p for source galaxies in eight different massive cluster fields, with photometric redshifts measured with at least five filters. The shear $\gamma_t(z)$ is normalized to the expected asymptotic value $\gamma_t(z = \infty)$. The points show the measured amplitude of the tangential shear profile, assuming a singular isothermal model for the cluster mass-density distributions. The solid curve in each plot shows the cosmological-distance–redshift relation for sources behind the cluster for our reference Λ-CDM cosmology (Ω_M=0.3, Ω_Λ=0.7, w=−1, h=0.7) normalized to fit the shear amplitude. The error bars on the measured values are the 68% uncertainties estimated from bootstrapped galaxy samples. The measured shear is based on galaxies for which BPZ ODDS > 0.5.

where $\overline{\Sigma}(< r)$ is the mean surface mass density inside radius r and $\overline{\Sigma}(r)$ is the azimuthally averaged surface mass density at radius r. Σ_c is the critical surface mass density,

$$\Sigma_c \equiv \frac{c^2}{4\pi G}\frac{D_S}{D_L D_{LS}}, \tag{11}$$

where D_S, D_L, and D_{LS} are the angular diameter distances from the observer to the lensed source galaxy, from the observer to the lens (the cluster), and from the lens to the source galaxy, respectively. The dependence of the weak gravitational shear on angular diameter distances is therefore

$$\gamma_t \propto \frac{D_{LS} D_L}{D_S}. \tag{12}$$

Since D_L is the same for all sources lensed by a given galaxy cluster, the dependence of shear on the source redshift is simply

$$\gamma_t \propto \frac{D_{LS}}{D_S} \equiv \beta(z).$$

Shape measurements yield an estimate for the reduced shear g rather than the shear γ; the two are related by

$$g = \frac{\beta_S \gamma_\infty}{1 - \beta_S \kappa_\infty}, \tag{13}$$

where

$$\beta_S = \frac{\beta(z_S)}{\beta_\infty}. \tag{14}$$

κ_∞ and γ_∞ are the convergence and shear, respectively, of a lensed source at $z = \infty$.

To estimate the actual reduced shear g from the measured shear $\hat{g}$, we use a linear shear correction with slope $m(r_h)$ and intercept c measured from STEP2 simulations (Massey et al. 2007a):

$$g = \frac{\hat{g} - c}{1 + m(r_h)}, \tag{15}$$

where $m(r_h)$ is a function of the object size r_h relative to the PSF size of the observation (see Papers I and III).

Taylor et al. (2007) projected the constraints on cosmological parameters that would be possible from a five-band optical survey of galaxy clusters with masses $M \approx 10^{15} M_\odot$. For a survey of fifty of the most massive low- to moderate-redshift galaxy clusters with five-band photometry and a median source galaxy redshift of $z = 0.7$, similar to this paper's sample, Taylor et al. (2007) forecast that the dark-energy equation-of-state parameter w may be constrained to within ± 0.6, after combination with a WMAP prior. This anticipated precision is for models that allow curvature and evolving w, and improved constraints will therefore be possible for a flat cosmology with a static value for w. For a five-band survey covering 10000 deg^2 with median source galaxy redshift of $z = 0.7$, Taylor et al. (2007) projected a constraint of $\Delta w = 0.0075$. Taylor et al. (2007) made the assumption that the errors of photometric redshifts are Gaussian and that any magnitude- or size-dependent bias in ground-based shear measurements can be controlled to $z = 1.5$.

In a number of pioneering efforts, an increase in shear signal has been observed with distance of the source galaxies behind groups or clusters. Wittman et al. (2001) plotted the measured shear against photometric redshift for the galaxies lensed by a massive cluster at $z = 0.276$ (see also Wittman et al. 2003). Kitching et al. (2007) combined a tomographic analysis of the A901/2 supercluster, with a cosmic-shear analysis of two randomly selected fields using COMBO-17 photometric redshift estimates. Medezinski et al. (2011) showed that the shear signal increases with distance of sources behind the A370, ZwCl0024+17, and RXJ1347-11 galaxy clusters, based on color cuts applied to three-filter Subaru imaging. Taylor et al. (2011) measured the redshift dependence of the weak lensing shear behind groups in the COSMOS field using HST images for shape measurements and the Ilbert et al. (2009) thirty-band photometric redshifts.

8.1 Tomographic Signal Behind Individual Massive Clusters

We first examine how, for individual clusters, the variation of measured shear with source redshift compares with the prediction for a fiducial Λ-CDM cosmology (Ω_M=0.3, Ω_Λ=0.7, w=−1, h=0.7).

To determine the shear signal as a function of redshift in each field, we bin galaxies with BPZ ODDS > 0.5 according to their most probable redshift z_p. We fit a singular isothermal shear (SIS) profile

$$\gamma_t(r, z \in z_i) = \frac{A_i}{r} \tag{16}$$

to the tangential shear γ_t of the galaxies in the ith redshift bin z_i, where r is the distance to the center of the galaxy cluster. We divide each amplitude A_i by the asymptotic value A_∞ at $z = \infty$ expected for the fiducial Λ-CDM cosmology:

$$\frac{\gamma_t(z \in z_i)}{\gamma_t(\infty)} = \frac{A_i}{A_\infty}. \tag{17}$$

Figure 12 shows the variation of $\gamma_t(z \in z_i)/\gamma(\infty)$ versus mean redshift for eight cluster fields with excellent filter coverage (Suprime-Cam $B_J V_J R_C I_C z^+$ and, in some cases, also MegaPrime $u^* g^* r^* i^* z^*$). The error bars are uncertainties we estimate from bootstrapped samples of galaxies. These comparisons show good agreement between the observed variation in $\gamma_t(z)/\gamma(\infty)$ with redshift and the expectation for the fiducial cosmology.

8.2 Tomographic Signal From a Stack of 27 Massive Clusters

For a cosmology with zero spatial curvature (i.e., a 'flat' universe), the angular diameter distance $D(z)$ is equal to the product of the comoving distance ω_z and the scale factor a_z,

$$D(z) = \omega_z \times a_z. \tag{18}$$

Taylor et al. (2011) used this relation to stack the measured shear as a function of distance for multiple lenses.

For a flat geometry, Equation 12 simplifies to

$$\gamma_t(z) \propto \frac{\omega_L(\omega_S - \omega_L)}{\omega_S(1 + z_L)}, \tag{19}$$

where ω_S and ω_L are comoving distances from the observer to the source and lens, respectively, and z_L is the redshift of the lens. Defining the ratio x of the two comoving distances ω_S and ω_L as

$$x = \omega_S/\omega_L, \tag{20}$$

we can express Equation 19 in terms of x:

$$\gamma_t(x) \propto \frac{\omega_L}{1 + z_L}(1 - \frac{1}{x}). \tag{21}$$

Therefore, in a flat universe, we can express the tangential shear ratio $\gamma_t(x)/\gamma_t(x = \infty)$ simply in terms of x:

$$\frac{\gamma_t(x)}{\gamma_t(x = \infty)} = 1 - \frac{1}{x}. \tag{22}$$

We note that $\gamma_t(x = \infty)$ is not physical for the reference cosmology, because the ratio of comoving distances x remains finite as the source redshift z approaches infinity.

When estimating $\gamma_t(x)/\gamma_t(x = \infty)$ for each galaxy, we divide

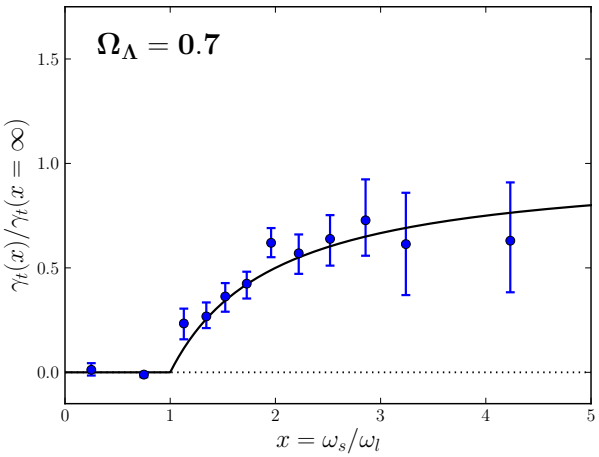

Figure 13. The stacked shear ratio for 27 clusters as a function of scaled comoving distance. The horizontal axis is the ratio of comoving distances from the observer to the source galaxy and to the lens. The vertical axis is the shear signal divided by that for a hypothetical (although physically disallowed) source at $x = \infty$ calculated for the fiducial cosmology and the best-fit cluster mass (from Paper III). The black curve is the predicted shear scaling $1 - 1/x$ for the reference cosmology. Points are the modes (maximum likelihood) measured from a Gaussian-kernel density estimator, and the error bars represent the 68% confidence interval as estimated from bootstrapped samples of galaxies in each bin.

the measured shear by the shear expected for a source galaxy at $x = \infty$ given the best-fit mass profile for the cluster (Paper III). We place the galaxies in the 27 cluster fields with photometry through at least the $B_J V_J R_C I_C z^+$ bands (see Table 1 of Paper I) into bins according to x. The value of $\gamma_t(x)/\gamma_t(x = \infty)$ for the sample of galaxies in each redshift bin is then estimated with a weighted Gaussian-kernel density estimator. Only the galaxies that are used to estimate cluster masses in Paper III are included; see that paper for a detailed description of the galaxy selection criteria. Galaxies are included only if the most probable photometric redshift is $z_p < 1.25$.

In Figure 13, the points correspond to the stacked shear signal calculated in the reference cosmology, and the error bars are estimated from bootstrapped galaxy samples at each redshift. The data show good qualitative agreement with the variation expected for the reference cosmology. We defer to a follow-up paper the determination of cosmological constraints from the tomographic lensing signal, using the entire redshift probability distribution $p(z)$ for each galaxy.

9 CONCLUSIONS

Converting the signal measured by CCD sensors mounted on a wide-field camera to calibrated AB magnitudes with better than several percent accuracy has typically required time-consuming calibration exposures as well as optimal observing conditions. When useful overlap with survey photometry is not available (e.g., limited dynamic range, color transformations from survey magnitudes), repeated standard-star observations in photometric conditions are necessary for accurate zeropoint calibration. Dedicated exposures sequences of dense stellar fields have been considered necessary to measure the position-dependent zeropoint error (~0.04-0.06 mag for SuprimeCam) present after correcting by dome or sky-flat calibration exposures.

For the Subaru and CFHT imaging that we analyzed, dedicated calibration data were not always available and conditions were not always photometric. We have developed improved tools that use only the instrumental stellar magnitudes in exposures of science targets to produce accurate star-flat models and color calibrations. These have sufficient power to enable high-quality photometric redshift estimates without spectroscopic training sets. We use 4735 galaxy spectra in 27 cluster fields across the sky to measure an accuracy of $\sigma((z_p - z_s)/(1 + z_s)) \approx 0.03$.

We achieve $\lesssim$ 0.01 - 0.02 mag color calibration by matching the observed stellar locus in color-color space to a model stellar locus. We developed a spectroscopic model for the dereddened SDSS stellar locus to estimate more accurately the locus expected for SuprimeCam and MegaPrime filters. This step is important because nonlinear color transformations exist between our SuprimeCam $B_J V_J R_C I_C z^+$ magnitudes and the SDSS $u'g'r'i'z'$ filters used to measure the stellar locus. We created a simple χ^2 GOF statistic that makes possible a solution for all unknown zeropoints simultaneously, without correlated errors. These improvements, including the correction of the SDSS stellar locus for Galactic extinction, were necessary to estimate robust and reliable photometric redshifts from our Subaru and CFHT imaging. Interested readers may find the Python code as well as a spectroscopic model for the locus at http://big-macs-calibrate.googlecode.com. Calibration requires only a catalog of stellar magnitudes and the total transmission function for each bandpass filter.

Summarizing the redshift posterior probability distribution $p(z)$ for each galaxy as a single redshift (e.g., the most probable redshift z_p) disregards any probability that the true galaxy redshift may have a very different value (e.g., catastrophic outliers). The $p(z)$ distribution contains more information than the most probable redshift, or other single-point estimates. We find good agreement between the stacked $\sum_{gal} p(z)$ and the redshift distribution estimated from thirty COSMOS photometric bands by Ilbert et al. (2009). The $p(z)$ distributions will provide a more powerful, less biased tool for science analysis than single-point estimates for ongoing and future surveys (e.g., PanSTARRS, Dark Energy Survey, SkyMapper, Large Synoptic Sky Survey).

The extreme gravitational potentials of massive galaxy clusters are expected to yield a simple, strong growth in shear signal with increasing distance of the source galaxy behind the cluster lens. The shape of the growth of shear behind a stack of 27 clusters with increasing redshift shows agreement with a fiducial Λ-CDM cosmology. The average shear we measure for foreground galaxies is consistent with zero.

The software we make available can produce state-of-the-art photometric accuracy without dedicated observations or the need to estimate nonlinear color terms. Stellar colors will be a useful tool for checking the accuracy of zeropoints obtained through ubercalibration of surveys (e.g., Ivezić et al. 2007; Padmanabhan et al. 2008; Schlafly et al. 2012) or close monitoring of atmospheric transparency (e.g., Burke et al. 2010; Blake & Shaw 2011).

ACKNOWLEDGMENTS

We thank F. William High, Jorg Dietrich, and Hendrik Hildebrandt for their expert advice and assistance on photometric calibration and redshift estimation. We also appreciate helpful discussions with Thomas Erben, C-J Ma, Daniel Coe, and Carlos Cunha.

This work is supported in part by the U.S. Department of Energy under contract number DE-AC02-76SF00515. This work was

also supported by the National Science Foundation under Grant Nos. AST-0807458 and AST-1140019. MTA and PRB acknowledge the support of NSF grant PHY-0969487. AM acknowledges the support of NSF grant AST-0838187. The authors acknowledge support from programs HST-AR-12654.01-A, HST-GO-12009.02-A, and HST-GO-11100.02-A provided by NASA through a grant from the Space Telescope Science Institute, which is operated by the Association of Universities for Research in Astronomy, Inc., under NASA contract NAS 5-26555. This work is also supported by the National Aeronautics and Space Administration through Chandra Award Numbers TM1-12010X, GO0-11149X, GO9-0141X , and GO8-9119X issued by the Chandra X-ray Observatory Center, which is operated by the Smithsonian Astrophysical Observatory for and on behalf of the National Aeronautics Space Administration under contract NAS8-03060. DEA recognizes the support of a Hewlett Foundation Stanford Graduate Fellowship.

Based in part on data collected at Subaru Telescope (University of Tokyo) and obtained from the SMOKA, which is operated by the Astronomy Data Center, National Astronomical Observatory of Japan. Based on observations obtained with MegaPrime/MegaCam, a joint project of CFHT and CEA/DAPNIA, at the Canada-France-Hawaii Telescope (CFHT), which is operated by the National Research Council (NRC) of Canada, the Institute National des Sciences de l'Univers of the Centre National de la Recherche Scientifique of France, and the University of Hawaii. This research used the facilities of the Canadian Astronomy Data Centre operated by the National Research Council of Canada with the support of the Canadian Space Agency. This research has made use of the VizieR catalogue access tool, CDS, Strasbourg, France. Funding for SDSS-III has been provided by the Alfred P. Sloan Foundation, the Participating Institutions, the National Science Foundation, and the U.S. Department of Energy Office of Science. The SDSS-III web site is http://www.sdss3.org/. This research has made use of the NASA/IPAC Extragalactic Database (NED), which is operated by the Jet Propulsion Laboratory, Caltech, under contract with NASA.

REFERENCES

Abrahamse, A., Knox, L., Schmidt, S., Thorman, P., Tyson, J. A., & Zhan, H. 2011, ApJ, 734, 36
Aihara, H., et al. 2011, ApJS, 193, 29
Applegate, D. E., et al. 2012, ArXiv e-prints
Arnouts, S., Cristiani, S., Moscardini, L., Matarrese, S., Lucchin, F., Fontana, A., & Giallongo, E. 1999, MNRAS, 310, 540
Baba, H., et al. 2002, Report of the National Astronomical Observatory of Japan, 6, 23
Barrett, E. 2006, PhD thesis, University of Hawai'i at Manoa
Baum, W. A. 1962, in IAU Symposium, Vol. 15, Problems of Extra-Galactic Research, ed. G. C. McVittie, 390–+
Benítez, N. 2000, ApJ, 536, 571
Bertin, E. & Arnouts, S. 1996, A&AS, 117, 393
Bertin, E., Mellier, Y., Radovich, M., Missonnier, G., Didelon, P., & Morin, B. 2002, in Astronomical Society of the Pacific Conference Series, Vol. 281, Astronomical Data Analysis Software and Systems XI, ed. D. A. Bohlender, D. Durand, & T. H. Handley, 228
Blake, C. H. & Shaw, M. M. 2011, PASP, 123, 1302
Burke, D. L., et al. 2010, ApJ, 720, 811
Capak, P., et al. 2007, ApJS, 172, 99
Capak, P. L. 2004, PhD thesis, University of Hawaii
Coe, D., Benítez, N., Sánchez, S. F., Jee, M., Bouwens, R., & Ford, H. 2006, AJ, 132, 926
Coleman, G. D., Wu, C.-C., & Weedman, D. W. 1980, ApJS, 43, 393
Coupon, J., et al. 2012, A&A, 542, A5
Covey, K. R., et al. 2007, AJ, 134, 2398
Cunha, C. E., Lima, M., Oyaizu, H., Frieman, J., & Lin, H. 2009, MNRAS, 396, 2379
Davis, T. A. 2006, Direct Methods for Sparse Linear Systems (SIAM Book Series on the Fundamentals of Algorithms)
Drimmel, R. & Spergel, D. N. 2001, ApJ, 556, 181
Ebeling, H., Barrett, E., Donovan, D., Ma, C.-J., Edge, A. C., & van Speybroeck, L. 2007, ApJ, 661, L33
Ebeling, H., Edge, A. C., & Henry, J. P. 2001, ApJ, 553, 668
Ebeling, H., Edge, A. C., Mantz, A., Barrett, E., Henry, J. P., Ma, C. J., & van Speybroeck, L. 2010, MNRAS, 407, 83
Erben, T., et al. 2009, A&A, 493, 1197
Erben, T., et al. 2005, Astronomische Nachrichten, 326, 432
Fu, L., et al. 2008, A&A, 479, 9
Gilbank, D. G., Gladders, M. D., Yee, H. K. C., & Hsieh, B. C. 2011, AJ, 141, 94
High, F. W., et al. 2010, ApJ, 723, 1736
High, F. W., Stubbs, C. W., Rest, A., Stalder, B., & Challis, P. 2009, AJ, 138, 110
Hoekstra, H., et al. 2006, ApJ, 647, 116
Ilbert, O., et al. 2006, A&A, 457, 841
Ilbert, O., et al. 2009, ApJ, 690, 1236
Ivezić, Ž., et al. 2004, Astronomische Nachrichten, 325, 583
Ivezić, Ž., et al. 2008, ApJ, 684, 287
Ivezić, Ž., et al. 2007, AJ, 134, 973
Jain, B. & Taylor, A. 2003, Physical Review Letters, 91, 141302
Jones, D. O., West, A. A., & Foster, J. B. 2011, AJ, 142, 44
Kalberla, P. M. W. & Kerp, J. 2009, ARA&A, 47, 27
Kinney, A. L., Calzetti, D., Bohlin, R. C., McQuade, K., Storchi-Bergmann, T., & Schmitt, H. R. 1996, ApJ, 467, 38
Kitching, T. D., Heavens, A. F., Taylor, A. N., Brown, M. L., Meisenheimer, K., Wolf, C., Gray, M. E., & Bacon, D. J. 2007, MNRAS, 376, 771
Koch, A., Odenkirchen, M., Caldwell, J. A. R., & Grebel, E. K. 2003, Astronomische Nachrichten Supplement, 324, 95
Kron, R. G. 1980, ApJS, 43, 305
Lilly, S. J., et al. 2009, ApJS, 184, 218
Lilly, S. J., Le Fevre, O., Crampton, D., Hammer, F., & Tresse, L. 1995, ApJ, 455, 50
LSST Science Collaborations, et al. 2009, ArXiv e-prints
Ma, C.-J., Ebeling, H., Donovan, D., & Barrett, E. 2008, ApJ, 684, 160
MacDonald, E. C., et al. 2004, MNRAS, 352, 1255
Magnier, E. A. & Cuillandre, J.-C. 2004, PASP, 116, 449
Manfroid, J., Selman, F., & Jones, H. 2001, The Messenger, 104, 16
Marshall, D. J., Robin, A. C., Reylé, C., Schultheis, M., & Picaud, S. 2006, A&A, 453, 635
Massey, R., et al. 2007a, MNRAS, 376, 13
Massey, R., et al. 2007b, ApJS, 172, 239
Medezinski, E., Broadhurst, T., Umetsu, K., Benítez, N., & Taylor, A. 2011, MNRAS, 414, 1840
Nelder, J. A. & Mead, R. 1965, Computer Journal, 7, 308
Padmanabhan, N., et al. 2008, ApJ, 674, 1217
Pickles, A. J. 1998, PASP, 110, 863
Regnault, N., et al. 2009, A&A, 506, 999
Schlafly, E. F., et al. 2012, ArXiv e-prints

Schlegel, D. J., Finkbeiner, D. P., & Davis, M. 1998, ApJ, 500, 525
Schrabback, T., et al. 2010, A&A, 516, A63+
Scoville, N., et al. 2007, ApJS, 172, 1
Sheldon, E. S., Cunha, C., Mandelbaum, R., Brinkmann, J., & Weaver, B. A. 2011, ArXiv e-prints
Taylor, A. N., Kitching, T. D., Bacon, D. J., & Heavens, A. F. 2007, MNRAS, 374, 1377
Taylor, J. E., et al. 2011, ArXiv e-prints
von der Linden, A., et al. 2012, ArXiv e-prints
West, A. A., et al. 2011, AJ, 141, 97
Williams, R. E., et al. 1996, AJ, 112, 1335
Wittman, D., Margoniner, V. E., Tyson, J. A., Cohen, J. G., Becker, A. C., & Dell'Antonio, I. P. 2003, ApJ, 597, 218
Wittman, D., Ryan, R., & Thorman, P. 2012, MNRAS, 421, 2251
Wittman, D., Tyson, J. A., Margoniner, V. E., Cohen, J. G., & Dell'Antonio, I. P. 2001, ApJ, 557, L89